

Department of Physics and Astronomy

University of Heidelberg

Master thesis

in Physics

submitted by

Patrick Fahner

born in Mannheim

September 2015

A study of the decay

$$\Lambda_b^0 \rightarrow D^0 p \mu^- \bar{\nu}_\mu X$$

with the LHCb experiment

This Master thesis has been carried out by (Name Surname)

at the

(institute)

under the supervision of

(Frau/Herrn Prof./Priv.-Doz. Name Surname)

(Titel der Masterarbeit - deutsch):

(Abstract in Deutsch, max. 200 Worte. Beispiel: [?])

Lorem ipsum dolor sit amet, consectetur adipiscing elit, sed eiusmod tempor incididunt ut labore et dolore magna aliqua. Ut enim ad minim veniam, quis nostrud exercitation ullamco laboris nisi ut aliquid ex ea commodo consequat. Quis aute iure reprehenderit in voluptate velit esse cillum dolore eu fugiat nulla pariatur. Excepteur sint obcaecat cupiditat non proident, sunt in culpa qui officia deserunt mollit anim id est laborum.

Duis autem vel eum iriure dolor in hendrerit in vulputate velit esse molestie consequat, vel illum dolore eu feugiat nulla facilisis at vero eros et accumsan et iusto odio dignissim qui blandit praesent luptatum zzril delenit augue duis dolore te feugait nulla facilisi. Lorem ipsum dolor sit amet, consectetur adipiscing elit, sed diam nonummy nibh euismod tincidunt ut laoreet dolore magna aliquam erat volutpat.

Ut wisi enim ad minim veniam, quis nostrud exercitation ullamcorper suscipit lobortis nisl ut aliquip ex ea commodo consequat. Duis autem vel eum iriure dolor in hendrerit in vulputate velit esse molestie consequat, vel illum dolore eu feugiat nulla facilisis at vero eros et accumsan et iusto odio dignissim qui blandit praesent luptatum zzril delenit augue duis dolore te feugait nulla facilisi.

(Title of Master thesis - english):

(abstract in english, at most 200 words. Example: [?])

Lorem ipsum dolor sit amet, consectetur adipiscing elit, sed eiusmod tempor incididunt ut labore et dolore magna aliqua. Ut enim ad minim veniam, quis nostrud exercitation ullamco laboris nisi ut aliquid ex ea commodo consequat. Quis aute iure reprehenderit in voluptate velit esse cillum dolore eu fugiat nulla pariatur. Excepteur sint obcaecat cupiditat non proident, sunt in culpa qui officia deserunt mollit anim id est laborum.

Duis autem vel eum iriure dolor in hendrerit in vulputate velit esse molestie consequat, vel illum dolore eu feugiat nulla facilisis at vero eros et accumsan et iusto odio dignissim qui blandit praesent luptatum zzril delenit augue duis dolore te feugait nulla facilisi. Lorem ipsum dolor sit amet, consectetur adipiscing elit, sed diam nonummy nibh euismod tincidunt ut laoreet dolore magna aliquam erat volutpat.

Ut wisi enim ad minim veniam, quis nostrud exercitation ullamcorper suscipit lobortis nisl ut aliquip ex ea commodo consequat. Duis autem vel eum iriure dolor in hendrerit in vulputate velit esse molestie consequat, vel illum dolore eu feugiat nulla facilisis at vero eros et accumsan et iusto odio dignissim qui blandit praesent luptatum zzril delenit augue duis dolore te feugait nulla facilisi.

Contents

1	Introduction	6
2	Theory and motivation	7
2.1	The Standard Model of Particle Physics	7
2.2	Baryons	7
2.3	Resonances	7
2.4	Analysis methods	7
2.4.1	Sidebandsubtraction	7
2.4.2	Wrong sign combinations	7
2.4.3	Corrected mass	7
2.4.4	Beeston-Barlow method	7
2.4.5	Binned likelihood fit	7
3	The LHCb detector	8
3.1	Tracking detectors	9
3.1.1	Vertex Locator (VELO)	9
3.1.2	Trigger Tracker / Tracker Turicensis (TT)	9
3.1.3	Inner Tracker (IT)	11
3.1.4	Outer Tracker (OT)	12
3.1.5	Track classification	12
3.2	Particle identification	12
3.2.1	Ring Imaging Cherenkov Detector (RICH)	12
3.2.2	Calorimeter system	12
3.2.3	Muon chambers	12
3.3	Trigger	12
3.3.1	L0-Trigger	12
3.3.2	High Level Trigger (HLT)	12
4	Analysis strategy	13
5	Data reconstruction and selection	14
5.1	Trigger requirements	14
6	Signal fit	16
6.1	Getting the fit parametrization	16
6.1.1	$\log \chi^2_{\text{IP}}$ shape	16
6.1.2	Control of $\log \chi^2_{\text{IP}}$ parametrization	18

6.1.3	$D^0 p$ mass shape	19
6.2	Determination of the massresolution	21
6.3	Nominal fit in two dimensions	22
6.4	Control of the method and parametrization	23
6.5	Extraction of $\Lambda_b^0 \rightarrow D^0 p \mu^- \bar{\nu}_\mu X$ signal yield together with $\Lambda_c(2880)^+$ and $\Lambda_c(2940)^+$ properties	25
7	Normalisation fit	27
7.1	Reduction and handling of backgrounds	27
7.1.1	Non Λ_c^+ background	27
7.1.2	Random combinations of Λ_c^+ and μ^-	28
7.1.3	Peaking backgrounds	28
7.2	Fit of the $p K^- \pi^+ \mu^-$ corrected mass	29
8	Efficiencies	32
8.1	Kinematic reweighting of the $\Lambda_b^0 \rightarrow D^0 p \mu^- \bar{\nu}_\mu X$ and $\Lambda_b^0 \rightarrow \Lambda_c^+ \mu^- \bar{\nu}_\mu$ channel	33
8.2	Reweighting of the $\Lambda_b^0 \rightarrow D^0 p \mu^- \bar{\nu}_\mu X$ decay simulation	34
8.3	Generator level efficiencies	35
8.4	Reconstruction and selection efficiencies	36
8.5	Total efficiencies	36
9	Backgrounds	37
9.1	Proton misidentification	37
9.1.1	Definition of PID particle regions - Number of particle candi- dates	38
10	Systematics	42
A	Massresolution	43
B	Reweighting of $\Lambda_b^0 \rightarrow D^0 p \mu^- \bar{\nu}_\mu X$ decay simulation	45

1 Introduction

2 Theory and motivation

2.1 The Standard Model of Particle Physics

2.2 Baryons

2.3 Resonances

2.4 Analysis methods

2.4.1 Sidebandsubtraction

2.4.2 Wrong sign combinations

2.4.3 Corrected mass

2.4.4 Beeston-Barlow method

2.4.5 Binned likelihood fit

3 The LHCb detector

Most parts of this chapter are taken from [1]

The LHCb experiment is one of the four big experiments, currently running at the Large Hadron Collider (LHC) of the European Organization for Nuclear Research CERN in Geneva, Switzerland. In contrast to the other three experiments – ATLAS and CMS are searching for direct hints of new physics, ALICE investigates the Quark-Gluon-Plasma – LHCb is dedicated to look indirectly for physics beyond the Standard Model (see section 2) by the study of hadrons containing either a heavy b - or c -quark.

...

The layout of the LHCb detector can be seen in figure 3.1. It is built as a single-arm forward spectrometer. The reason for this choice is, that at LHC energies of $\sqrt{s} = 14 \text{ TeV}$ at the maximum, b - and \bar{b} - hadrons are predominantly produced in the forward (or backward) region.

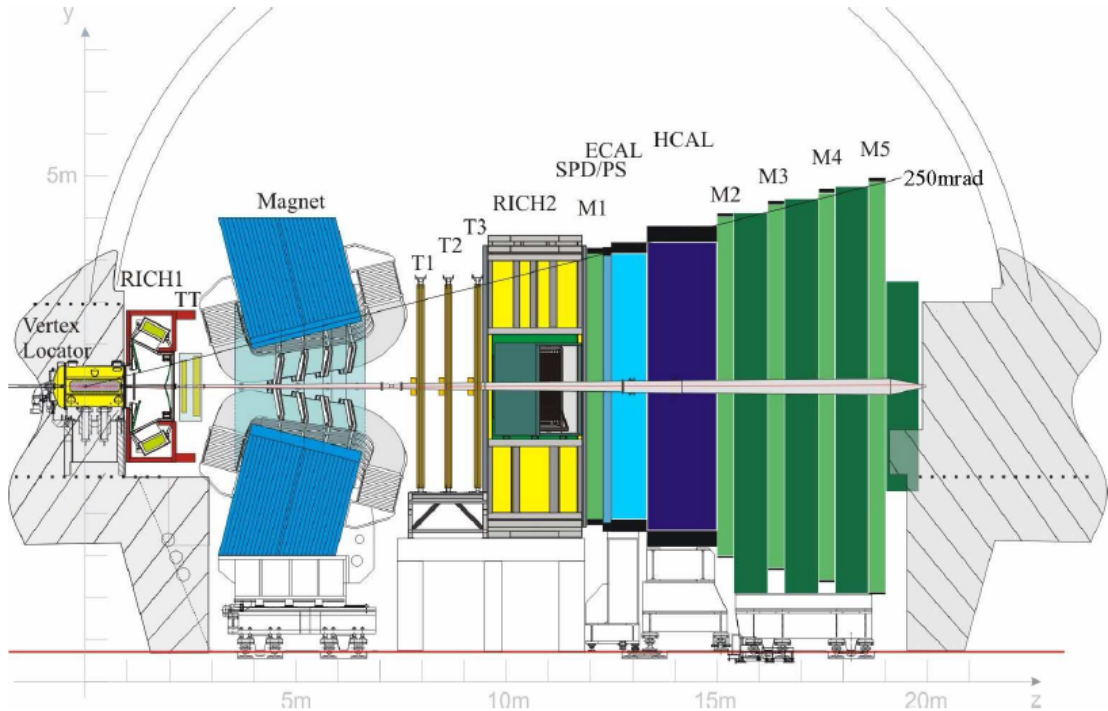


Figure 3.1: The LHCb detector.

3.1 Tracking detectors

Tracking describes the whole procedure to reconstruct the trajectories of the (charged) particles produced in the proton-proton collision. If there's a magnet in use, the particles' charges and momenta can be determined as well. For that purpose, a system of several subdetectors is aligned up- and downstream the dipole magnet, namely the Vertex locator (VELO), the Trigger Tracker (TT) and the Trigger stations (T1-T3) built-up by the Inner Tracker (IT) and the Outer Tracker (OT).

3.1.1 Vertex Locator (VELO)

The VERtex LOcator (VELO) is placed directly around the primary interaction point. Its task is to precisely measure the track coordinates of charged particles and separate the proton-proton interaction point from other vertices, namely either other primary vertices (so called pile-up events) or secondary vertices. The latter ones are typically for b - or c -hadron decays [2] and a good separation and resolution of these vertices is crucial for the LHCb physics programme. As an example serves the measurement of particles' decay length and time for the determination of the rapid $B_s^0 - \bar{B}_s^0$ oscillation frequency [3].

The VELO is built up by silicon modules due to the high particle flux and thus high radiation in the interaction region. It is placed only 7 mm apart from the beam. This is closer than the required aperture of the LHCb beam pipe at injection. Thus, the VELO sensors are made of silicon microstrips shaped as slightly overlapping half-discs. The two halves can be moved in x - and y -direction to avoid radiation damages unless the beam is stable.

Each module provides a measurement of the r - and ϕ -coordinates. The sensors for these measurements are correspondingly called R - and Φ -sensor, which can be seen in figure 3.2. An overview over the VELO system with its modules is shown in figure 3.3. Around the nominal interaction region, the modules are placed closer to each other. Upstream there are two R sensors dedicated to veto pile-up events. Figure 3.3 furthermore shows the VELO in closed and opened position. With this setup the VELO reaches a track finding efficiency above 98%. Its resolution on vertices is $13\text{ }\mu\text{m}$ in the transverse plane and $71\text{ }\mu\text{m}$ along the beam axis for vertices with 25 tracks. The resolution on the impact parameter is smaller than $35\text{ }\mu\text{m}$ for particles with a transverse momentum larger than 1 GeV [1, 2, 4].

3.1.2 Trigger Tracker / Tracker Turicensis (TT)

The Tracker Turicensis or formerly the Trigger Tracker is located in front of the entrance of the LHCb magnet. It is used for several tasks:

- deliver transverse momentum information for Level-1 trigger,
- reconstruct trajectories of long-lived neutral particles decaying outside the VELO

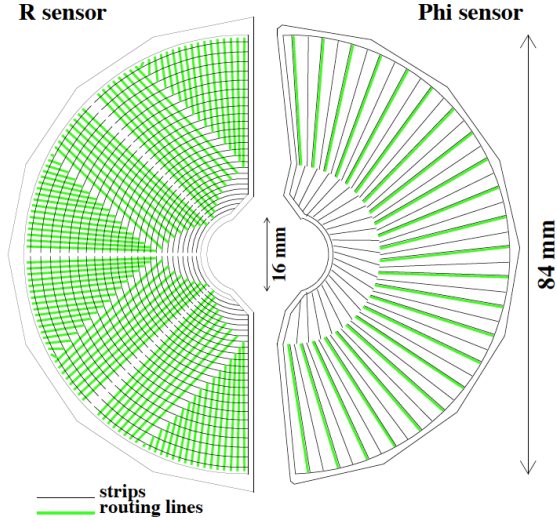


Figure 3.2: Schematic representation of an R and a Φ sensor. The R sensor strips are arranged into four approximately 45° segments and have routing lines perpendicular to the strips. The Φ sensor has two zones with inner and outer strips. The routing lines of the inner strips are orientated parallel to the outer strips. Figure and caption taken from [4].

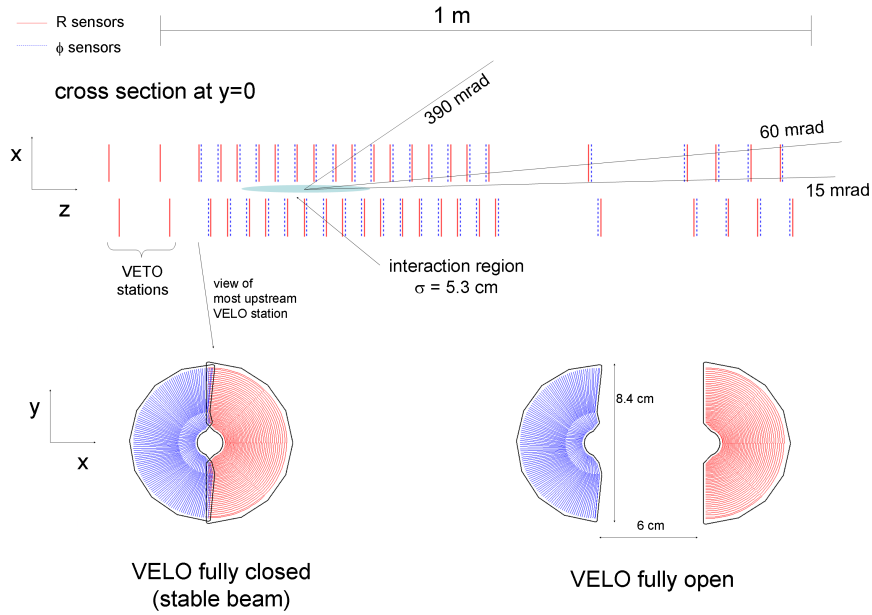


Figure 3.3: Cross section in the (x, z) plane of the VELO silicon sensors, at $y = 0$, with the detector in the fully closed position. The front face of the first modules is also illustrated in both the closed and open positions. The two pile-up veto stations are located upstream of the VELO sensors. Figure and caption taken from [1].

- reconstruct low-momenta particles bent out by the magnet before reaching the station T1-T3.

The TT makes completely use of silicon microstrip detector. It consist of one station made of four planes along the beam axis. The first and the fourth layer have vertical readout strips (x -layer), while the second and third are rotated by an angle $\pm 5^\circ$ to get a high resolution in the bending plane and additional information in y -direction. Between the u and v layer there is a gap of around 30 cm. Figure 3.4 shows schematically the layout of the TT.

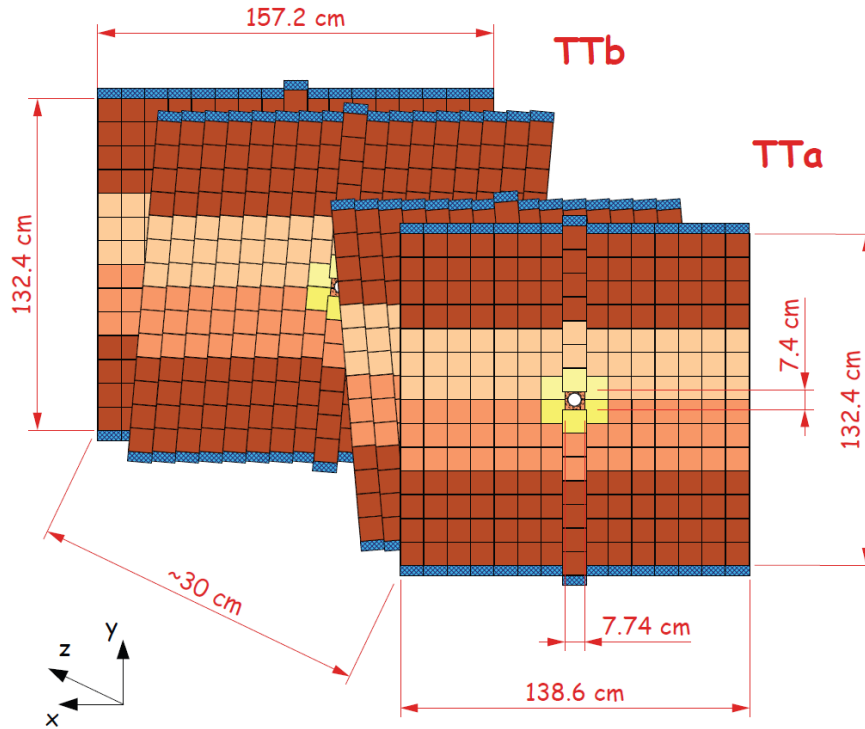


Figure 3.4: Layout of the Tracker Turicensis (TT). Figure taken from [5].

3.1.3 Inner Tracker (IT)

Being a silicon micro-strip detector, the Inner Tracker (IT) uses the same technology as the TT. It builds the inner part of the three tracking stations T1-T3 (see figure 3.1). Each station consists of four boxes as shown in figure 3.5. In each box there are again 4 layers, two vertical and two stereo, analogously to the TT [1, 5].

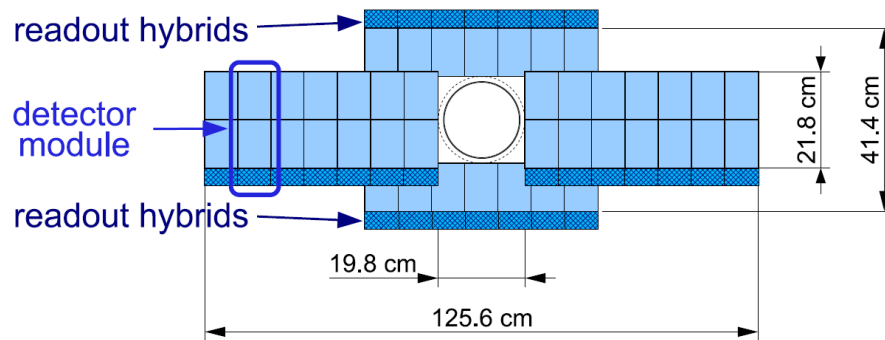


Figure 3.5: Layout of a x detection layer in the second Inner Tracker (IT) station.
Figure taken from [1].

3.1.4 Outer Tracker (OT)

3.1.5 Track classification

3.2 Particle identification

3.2.1 Ring Imaging Cherenkov Detector (RICH)

3.2.2 Calorimeter system

3.2.3 Muon chambers

3.3 Trigger

3.3.1 L0-Trigger

3.3.2 High Level Trigger (HLT)

4 Analysis strategy

$$\mathcal{R} = \frac{\mathcal{B}(\Lambda_b^0 \rightarrow D^0 p \mu^- \bar{\nu}_\mu X)}{\mathcal{B}(\Lambda_b^0 \rightarrow \Lambda_c^+ \mu^- \bar{\nu}_\mu)} = \frac{N_{D^0 p}}{N_{\Lambda_c^+}} \cdot \frac{\epsilon_{\Lambda_c^+}}{\epsilon_{D^0 p}} \cdot \frac{\mathcal{B}(\Lambda_c^+ \rightarrow p K^- \pi^+)}{\mathcal{B}(D^0 \rightarrow K^- \pi^+)}. \quad (4.1)$$

5 Data reconstruction and selection

The analysis of the decays $\Lambda_b^0 \rightarrow D^0 p \mu^- \bar{\nu}_\mu X$ (signal channel) and $\Lambda_b^0 \rightarrow \Lambda_c^+ \mu^- \bar{\nu}_\mu$ (normalization channel) requires the reconstruction and selection of possible signal candidates. The term “signal candidates” implies, that a data sample doesn’t contain only the desired signal events after reconstruction and selection, but is also polluted by events from different sources, albeit looking like signal. These backgrounds can have several reasons: One possibility is that the final state particles are randomly combined but fulfil all the applied criteria. This kind of background is also known as combinatoric background. There are furthermore the so-called physical backgrounds. With this term one summarises physical decays where one either misidentifies a final state particle or only partially reconstruct an event und thus leading to a wrong interpretation of the decay. As an example for the misidentification consider the decay $\Lambda_b^0 \rightarrow D^0 p \pi^-$. If the π^- is now misidentified as a muon this decay looks exactly like the signal channel of this analysis. Partially reconstructed events play an important role in the normalisation channel $\Lambda_b^0 \rightarrow \Lambda_c^+ \mu^- \bar{\nu}_\mu$. There exists also semileptonic Λ_b^0 decays into excited Λ_c^{*+} states, $\Lambda_b^0 \rightarrow \Lambda_c^{*+} \mu^- \bar{\nu}_\mu$. Subsequently, these excited Λ_c^{*+} states decay into an Λ_c^+ and additional pions or photons. If one misses these pions and photons the decay looks exactly like $\Lambda_b^0 \rightarrow \Lambda_c^+ \mu^- \bar{\nu}_\mu$.

Since such misidentified decays or combinatoric backgrounds distort the measurement of physical quantities, the event reconstruction and above all the selection aims to reduce these backgrounds as much as possible while keeping as much signal as possible. At LHCb, this procedure is done in several steps, described for the present analysis in this chapter, namely the Trigger, the preselection (or stripping) and the offline selection. Nonetheless not every background source can be easily eliminated. The handling of such issues is part of chapter 9.

5.1 Trigger requirements

Trigger requirements are already applied during data taking to reduce the arising data to a recordable amount. There exists so called trigger lines for different physics purposes. These trigger lines then contain the requirements on the particles’ properties.

Due to their large lifetime and their little interaction with matter muons leave a very clean signal in the detector and are the best suited to trigger on. For the $\Lambda_b^0 \rightarrow D^0 p \mu^- \bar{\nu}_\mu X$ channel the muon has pass the L0Muon_TOS line at L0 level. TOS is

the abbreviation for Trigger On Signal, i.e. the presence of the signal is sufficient to generate a positive trigger decision [6]. To record an event this line requires that the transverse momentum of at least one muon candidate is larger than 1760 MeV¹. At Hlt1 two different trigger lines are applied. The Hlt1TrackMuon_TOS line requires the muon candidate to have at least one hit in the VELO and triggers on the track quality.

¹This requirement changed between 2011 and 2012. For a better readability only the 2012 trigger settings are described here. The 2011 configuration can be found in [?].

6 Signal fit

This chapter describes the way how the signal yield $N_{A_c^+}$ of the signal channel $A_b^0 \rightarrow D^0 p \mu^- \bar{\nu}_\mu X$ is derived. As already explained in section 4 the aim is to perform a twodimensional fit in the $D^0 p$ mass and $\log \chi_{\text{IP}}^2$ distribution. The $\log \chi_{\text{IP}}^2$ distribution enables the fit to distinguish (nonresonant) signal from random proton background. This information is used in the $M(D^0 p)$ dimension to separate the different components and to learn more about the $M(D^0 p)$ spectrum. From other experiments it is expected that there should appear the two resonances $A_c(2880)^+ \rightarrow D^0 p$ and $A_c(2940)^+ \rightarrow D^0 p$ [7]. Before the fit can be performed, a proper parametrization of the fit components has to be found. This will be described in the following section.

6.1 Getting the fit parametrization

Different approaches are used to model the components of the fit. The discussion will be separated in the two fit dimensions starting with the $\log \chi_{\text{IP}}^2$ shape.

6.1.1 $\log \chi_{\text{IP}}^2$ shape

For both, $\log \chi_{\text{IP}}^2$ signal and background components, simulations are used. The signal part can be described by a sum of two Bifurcated Gaussians. A Bifurcated is like a Gaussian, but with two different widths for the left and the right part from the maximum and thus providing an “asymmetric Gaussian”. If $\mathcal{G}(m|m_0, \sigma)$ denotes a usual Gaussian with mean m_0 and width σ , a Bifurcated Gaussian can be written as¹

$$\text{BfG}(m|m_0, \sigma_L, \sigma_R) \propto \begin{cases} \mathcal{G}(m|m_0, \sigma_L) & \text{for } m < m_0 \\ \mathcal{G}(m|m_0, \sigma_R) & \text{for } m > m_0 \end{cases}, \quad (6.1)$$

and the sum of two is in the following called a double Bifurcated Gaussian DBfG

$$\text{DBfG}(m|m_0, \vec{\sigma}_L, \vec{\sigma}_R, f_{\text{BfG}_1}) \propto \quad (6.2)$$

$$f_{\text{BfG}_1} \text{BfG}(m|m_0, \sigma_{L_1}, \sigma_{R_1}) + (1 - f_{\text{BfG}_1}) \text{BfG}(m|m_0, \sigma_{L_2}, \sigma_{R_2}), \quad (6.3)$$

where f_{BfG_1} denotes the fraction of the first BfG and the two BfGs share a common mean m_0 . The fit result on the signal simulation can be seen in figure 6.1.

¹All fit functions in the following are given without normalisation factors. That's why there always appears a \propto sign instead of an equal sign.

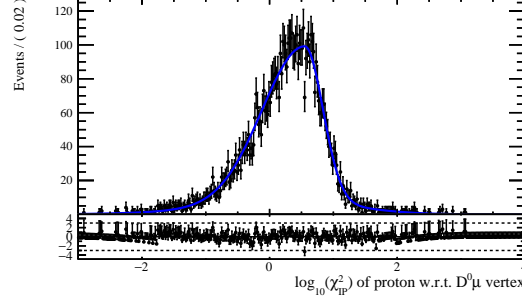


Figure 6.1: Fit to the $\log \chi_{\text{IP}}^2$ distribution of the signal simulation. As parametrization a double Bifurcated Gaussian has been chosen.

Concerning the background shape only a simulation with very few statistics is available. To get a better idea of the background $\log \chi_{\text{IP}}^2$ shape right sign and wrong sign events of this sample have been added. Since in this case they are both backgrounds with respect to the $\log \chi_{\text{IP}}^2$ signal it is assumed that their shapes are similar as figure 6.2 confirms. As fitfunction a single CrystalBall function is chosen. This function was first used by the CrystalBall collaboration to account for radiative losses in J/ψ or $\psi(2S)$ decays [8]. It is defined as

$$\text{CB}(m|m_0, \sigma, \alpha, n) \propto \begin{cases} \exp\left(-\frac{(m-m_0)^2}{2\sigma^2}\right) & \text{for } \frac{m-m_0}{\sigma} > -\alpha \\ A \cdot \left(B - \frac{m-m_0}{\sigma}\right)^{-n} & \text{for } \frac{m-m_0}{\sigma} \leq -\alpha \end{cases}, \quad (6.4)$$

where (6.5)

$$A = \left(\frac{n}{|\alpha|}\right)^n \exp\left(-\frac{|\alpha|^2}{2}\right), \quad (6.6)$$

$$B = \frac{n}{|\alpha|} - |\alpha|. \quad (6.7)$$

The CrystalBall function is hence a Gaussian with a power law tail. The result of the fit to the background simulation can be seen in figure 6.3.

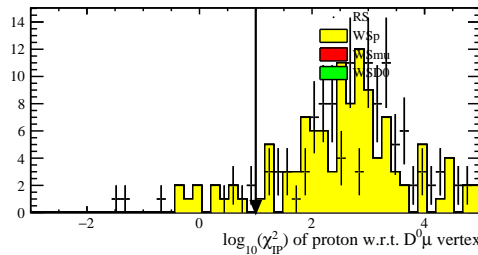


Figure 6.2: Comparison of RS and WS events in the background MC. Both, RS and WS shapes are very similar and can thus be added to increase statistics.

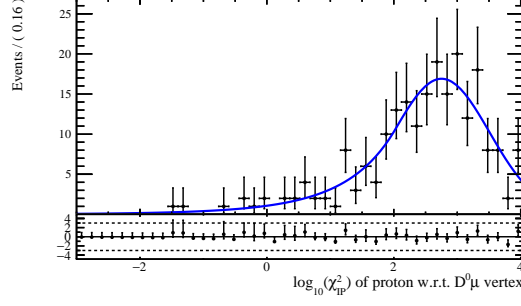


Figure 6.3: Fit to the (RS and WS added) $\log \chi_{\text{IP}}^2$ shape of the background simulation.

6.1.2 Control of $\log \chi_{\text{IP}}^2$ parametrization

As a control of the chosen parametrization of $\log \chi_{\text{IP}}^2$ for signal and background, a onedimensional fit on data is performed. This fit is later also used for systematic studies, since it is already able to distinguish between signal and background yields. The fitresult with the models mentioned above can be seen in figure 6.4 and the corresponding yields and parameter values in table 6.1. The chosen model nicely describes the data.

Table 6.1: Results of the onedimensional $\log \chi_{\text{IP}}^2$ fit on data.

Variable	Value
Yields	
signal yield	$(2.325 \pm 0.028) \cdot 10^4$
background yield	$(1.086 \pm 0.026) \cdot 10^4$
Signal (DBfG)	
mean	$(4.59 \pm 0.26) \cdot 10^{-1}$
left width 1	$(8.72 \pm 0.56) \cdot 10^{-1}$
right width 1	$(5.74 \pm 0.44) \cdot 10^{-1}$
left width 2	$(4.72 \pm 0.55) \cdot 10^{-1}$
right width 2	$(3.37 \pm 0.23) \cdot 10^{-1}$
fraction BfG 1	$(5.61 \pm 0.89) \cdot 10^{-1}$
Background (CB)	
CB mean	$(2.6 \pm 0.017) \cdot 10^0$
CB σ	$(6.85 \pm 0.14) \cdot 10^{-1}$
CB α	$(2.035 \pm 0.099) \cdot 10^0$
CB n	$(1.62 \pm 0.45) \cdot 10^0$

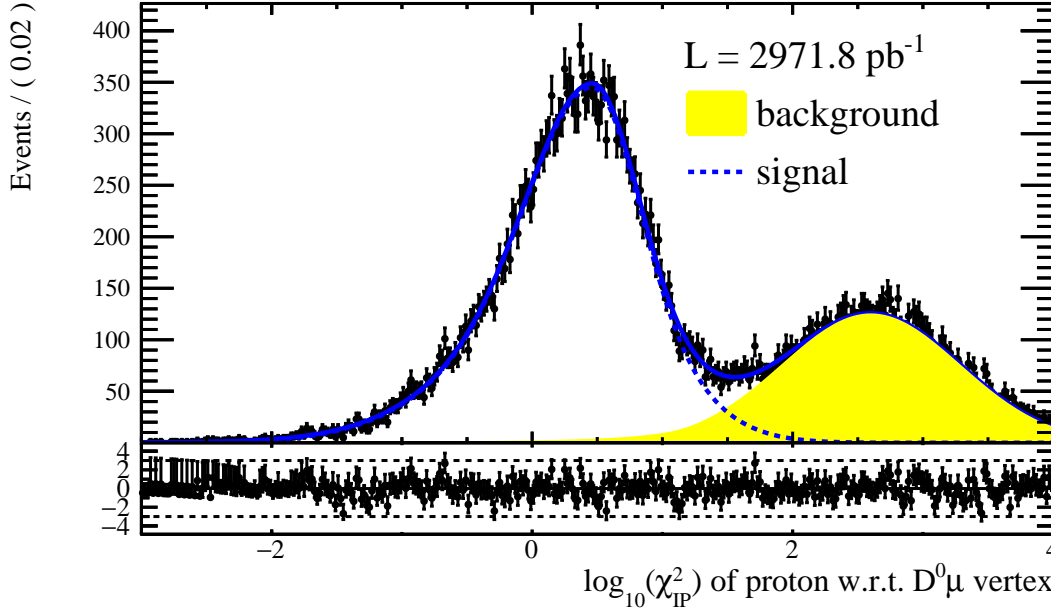


Figure 6.4: Fit to the $\log \chi_{\text{IP}}^2$ distribution of the data sample.

6.1.3 $D^0 p$ mass shape

To get an idea of the (random) background shape, events with a wrong sign (WS) proton are fitted since the transition from Λ_b^0 to a $D^0 \bar{p} \mu^-$ final state is physically forbidden by charge conservation and should thus give a good hint for randomly combined $\Lambda_b^0 \rightarrow D^0 p \mu^- \bar{\nu}_\mu$ candidates. The distribution is modeled with an empirical background function as

$$\text{EBG}(m|p, c_i) = \text{PS}(m|m_1, m_2) \cdot (m - m_0)^p \cdot \exp \left[c_1 \left(1 - \frac{m_0}{m} \right) + c_2^2 \left(1 - \frac{m_0}{m} \right)^2 \right], \quad (6.8)$$

where $m_0 := m_1 + m_2$ denotes the kinematic $D^0 p$ mass threshold and PS the phase space function

$$\text{PS}(m|m_1, m_2) = \frac{1}{2m} \sqrt{[m^2 - (m_1 + m_2)^2] [m^2 - (m_1 - m_2)^2]} \quad (6.9)$$

Figure 6.5 shows the result of the fit. No structure is observed in the WS mass spectrum.

Unfortunately, there isn't any reliable simulation predicting the mass shape for the $D^0 p$ invariant mass. A shape for the signal therefore has to be determined empirically. The $D^0 p$ mass is fitted with the requirement that the $D^0 p \mu$ system makes a good

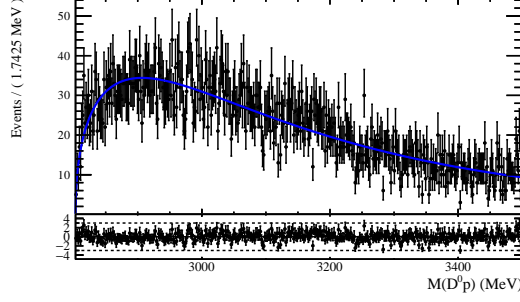


Figure 6.5: Fit to $D^0 p$ mass of WS proton events.

vertex, i.e. $\log \chi_{\text{IP}}^2 < 1$. This is a very signal rich region and should give a proper idea of the mass shape. The main part of the signal will be nonresonant but furthermore it is expected to see at least two resonances, namely the decays $\Lambda_c(2880)^+ \rightarrow D^0 p$ and $\Lambda_c(2940)^+ \rightarrow D^0 p$. These two resonances are parametrized by a relativistic Breit-Wigner distribution convoluted with a Gaussian $\mathcal{G}(m|m_0, \sigma)$ to account for the detector's mass resolution.

$$\text{RelBW}(m|m_0, \Gamma) = \left[2m \cdot \text{PS}(m|m_1, m_2) \cdot \frac{1}{(m^2 - m_0^2)^2 + m_0^2 \Gamma^2} \right] \otimes \mathcal{G}(m|m_0, \sigma), \quad (6.10)$$

Here PS denotes the phase space function of eq (6.9), m_0 the resonance's mass and Γ its width. The determination of the mass resolution is described in section 6.2. The obtained resolution is then fixed in all fits.

The nonresonant signal part is modeled with the sum of two exponentials multiplied by a turnon function.

$$\text{TDExp}(m|m_0, c_0, c_1, c_2, f_{c_1}) = (1 - e^{c_0(m-m_0)}) \cdot [f_{c_1} e^{c_1 m} + (1 - f_{c_1}) e^{c_2 m}] \quad (6.11)$$

This choice of turnon guarantees the function to rise as steep as necessary at $D^0 p$ mass threshold.

When fitting the $D^0 p$ mass it turns out, that this parametrization is not sufficient to describe the whole mass spectrum (see figure 6.6 left). There is an enhancement at low $D^0 p$ masses right after threshold. Different models for the nonresonant component have been tried to describe this steep curvature without success. A possible solution seems to be adding another component parametrized like the two resonances in the fit (fig. 6.6 right). With this choice the fit converges and describes the data well. The total fit function consists now of 4 parts: The nonresonant part modeled with the "turnon double exponential" function TDExp of eq. (6.11), the $\Lambda_c(2880)^+$, $\Lambda_c(2940)^+$ and a low mass enhancement, each modeled with a relativistic Breit-Wigner according eq. (6.10). The fit results can be seen in figure 6.6 (right) and table ??.

Note that at this point, there is no special motivation to introduce this component (and model it like the resonances) except to get a converging and data matching fit. There are several possible reasons for such an enhancement. A thorough discussion, if this additional component is actually needed and what its origins could be can be found in section ???. In the following this component will be treated as signal since it appears very clear in the signal rich, i.e. low $\log \chi^2_{\text{IP}}$ region and should does make a good decay vertex.

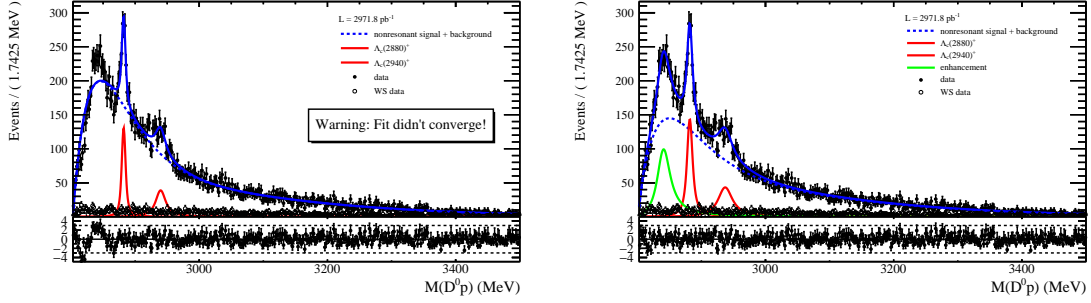


Figure 6.6: 1D fit of the $D^0 p$ mass distribution for $\log \chi^2_{\text{IP}} < 1$. The left side shows a fit with two resonances and a nonresonant part. Different attempts have been made to get a proper and converging fit. This issue can be solved by adding an additional component (right figure, green line), here parametrized like the two resonances.

6.2 Determination of the massresolution

If one sees a resonance in a mass spectrum, it isn't usually the natural width of a resonance which is seen. The reason lies in the fact that the detector has a finite massresolution "overlapping" the natural width. In this analysis the effect is accounted for by convoluting the Breit-Wigner, which is assumed to be the natural shape of the resonance, with a Gaussian, describing the smearing of the resonance due to massresolution.

The determination of the massresolution makes use of a simulation. For that purpose, the $D^0 p$ mass spectrum is split up in bins of 30 MeV. For each mass bin a histogram is filled with the difference of the generated (also called "true") and the reconstructed mass in the simulation. It is expected that this difference peaks around zero. Finally, a fit is performed on these histograms using a simple Gaussian function. The width of this Gaussian is then assumed to be the massresolution in the particular bin. Figure 6.7 shows on the left side exemplarily the massdifference between reconstructed and generated mass together with the fit in the bin $2863 < M(D^0 p) < 2893 \text{ MeV}$. The fits of all bins can be seen in Appendix ??, figure A.1. On the right side, the obtained massresolutions for all bins are plotted. The higher

Table 6.2: Results of the D^0p mass fit.

Variable	Value
Yields	
$\Lambda_c(2880)^+$ signal yield	$(1.26 \pm 0.16) \cdot 10^3$
$\Lambda_c(2940)^+$ signal yield	$(1.01 \pm 0.32) \cdot 10^3$
mass enhancement yield	$(2.12 \pm 0.44) \cdot 10^3$
nonresonant yield	$(1.652 \pm 0.078) \cdot 10^4$
$\Lambda_c(2880)^+$ resonance	
mean	$(2.88185 \pm 0.00035) \cdot 10^3$
width	$(8.9 \pm 1.4) \cdot 10^0$
$\Lambda_c(2940)^+$ resonance	
mean	$(2.9368 \pm 0.0021) \cdot 10^3$
width	$(2.62 \pm 0.79) \cdot 10^1$
Low mass enhancement	
mean	$(2.84012 \pm 0.0009) \cdot 10^3$
width	$(2.44 \pm 0.37) \cdot 10^1$
nonresonant part	
turn on mass threshold	$(2.80117 \pm 0.00051) \cdot 10^3$
turn on slope	$(-2.0 \pm 32.0) \cdot 10^{-5}$
exponential 1 slope	$(-2.34 \pm 0.13) \cdot 10^{-2}$
exponential 2 slope	$(-7.07 \pm 0.2) \cdot 10^{-3}$
fraction exponential 1	$(7.4 \pm 0.24) \cdot 10^{-1}$

the bin, the larger the errors are due to less statistics in these bins. Since only the bins containing the resonances are of particular interest, these larger errors doesn't matter for this study.

Regarding these results, the $\Lambda_c(2880)^+$, $\Lambda_c(2940)^+$ and the enhancement are fitted with the following fixed mass resolutions:

$$\begin{aligned}
\Lambda_c(2880)^+ : & \quad \sigma_{M, \Lambda_c(2880)^+} = (1.651 \pm 0.082) \text{ MeV}, \\
\Lambda_c(2940)^+ : & \quad \sigma_{M, \Lambda_c(2940)^+} = (1.97 \pm 0.11) \text{ MeV}, \\
\text{enhancement} : & \quad \sigma_{M, \text{enhancement}} = (1.254 \pm 0.055) \text{ MeV}.
\end{aligned}$$

6.3 Nominal fit in two dimensions

With a twodimensional fit of the D^0p mass and the $\log \chi_{\text{IP}}^2$ distribution it is possible to distinguish between nonresonant signal and background in the D^0p mass spectrum as already explained. Thus the different pieces of the previous sections are now put together for a fit of both distributions.

It is assumed that the $\log \chi_{\text{IP}}^2$ distribution is the same for all 4 different signal components (nonresonant signal, $\Lambda_c(2880)^+$, $\Lambda_c(2940)^+$, enhancement). This as-

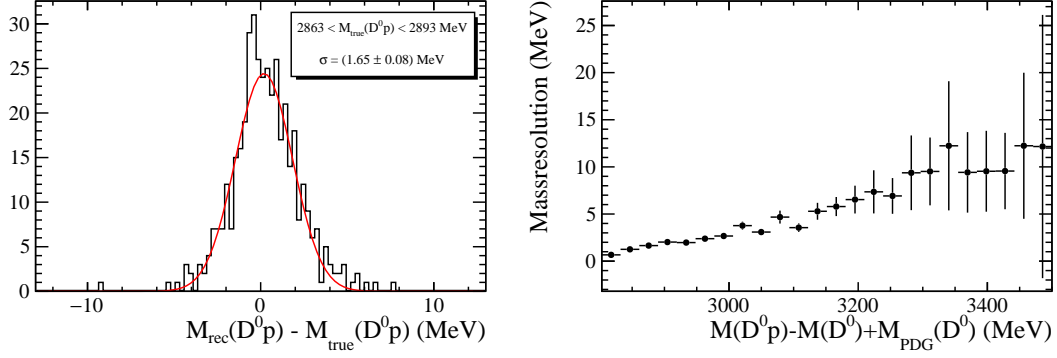


Figure 6.7: Left: Fit of a Gaussian to the difference between generated and reconstructed $D^0 p$ mass (simulation sample) in the range $2863 < M(D^0 p) < 2893$ MeV. The width of the Gaussian is taken as massresolution. Right: Obtained massresolutions for all bins. The large errors in the higher bins doesn't matter for the desired purpose as only the bins containing the resonances are relevant.

sumption bases on the fact that the decay topology should be the same in all cases². Hence, their $\log \chi^2_{\text{IP}}$ distributions share all parameters. For the $\log \chi^2_{\text{IP}}$ signal part a double Bifurcated Gaussian DBfG is chosen, whereas the background is modeled by a CrystalBall function CB. The $D^0 p$ mass' signal components are modeled with the same parametrization as described in section ???. The empiric background function EBG is used to describe the background.

Table 6.3 summarizes the parametrization of the entire twodimensional fit. The results of the fit are shown in table 6.4 and the projections can be seen in figure 6.8.

Table 6.3: Summary of the parameterization of the 2D fit

subset	mass distribution	logIP distribution
non-resonant signal	TDExp (eq. 6.11)	Double Bifurcated Gaussian
$A_c(2880)^+$ resonance	RelBW (eq. 6.10)	
$A_c(2940)^+$ resonance	RelBW (eq. 6.10)	
enhancement	RelBW (eq. 6.10)	
background	EBG (eq. 6.8)	CrystalBall

6.4 Control of the method and parametrization

As a control the two dimensional fit is performed for the WS data with the same parametrization as for the RS in section 6.3. However, since there shouldn't be any resonances, these two components and the enhancement have been omitted. The

²Presumed, that the enhancement indeed emerges to be a resonance or another signal component.

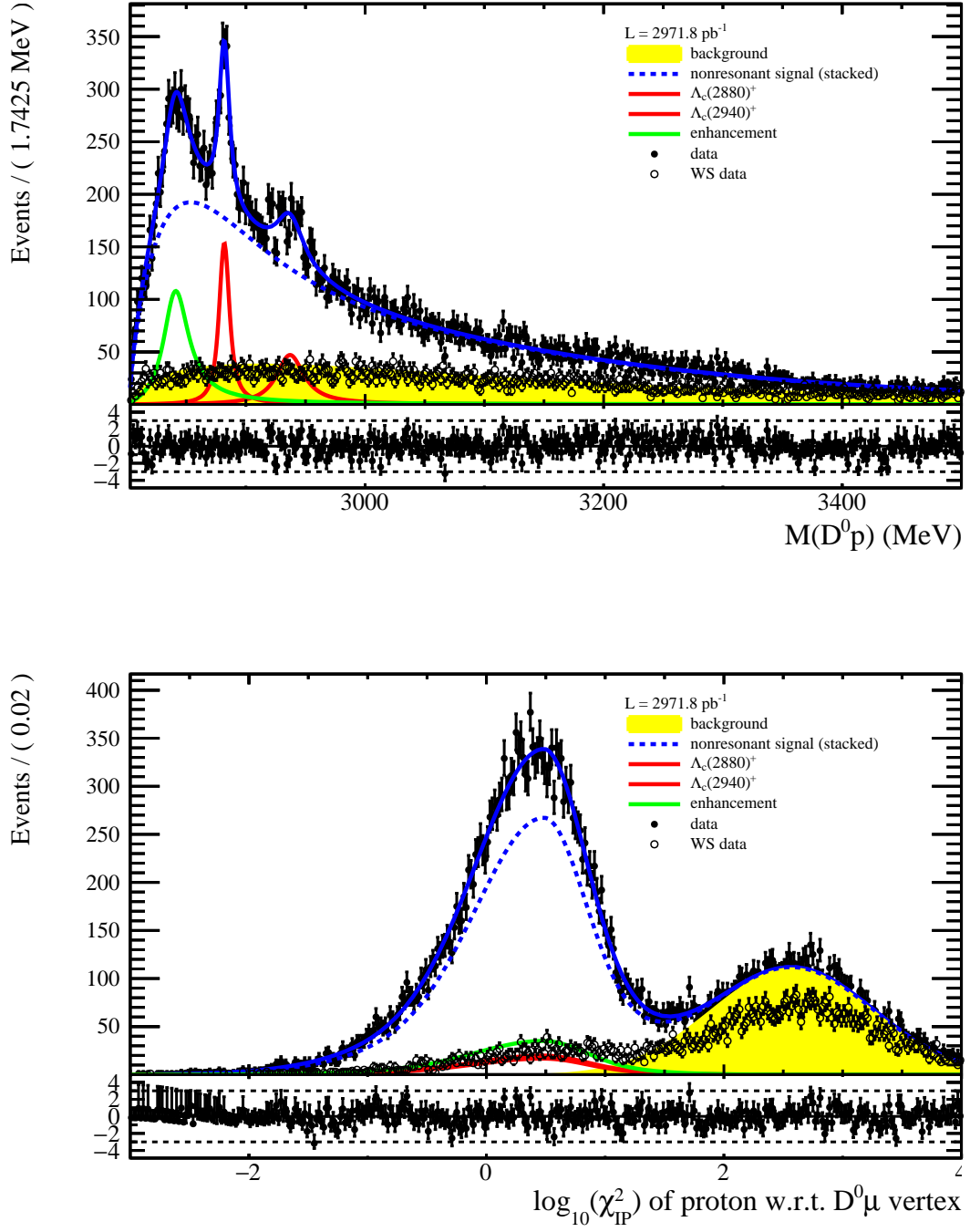


Figure 6.8: Twodimensional fit on the $\Lambda_b^0 \rightarrow D^0 p \mu^- \bar{\nu}_\mu X$ candidates. There are shown the $D^0 p$ mass (top) and $\log \chi^2_{\text{IP}}$ (bottom) projection. The total fit parametrization is summarized in table 6.3.

respective plots can be seen in figure ?? . No structure in the mass distribution is seen. This means that the identification of the $\Lambda_c(2880)^+$ and $\Lambda_c(2940)^+$ in the D^0p mass spectrum seems to be appropriate. Interesting is to note, that besides the two resonances even the enhancement vanishes. It can't thus be explained by random combinations of the particles. Concerning the $\log \chi_{\text{IP}}^2$ distribution, there is nevertheless a "signal-like" part which has to be discussed in the backgrounds chapter 9.

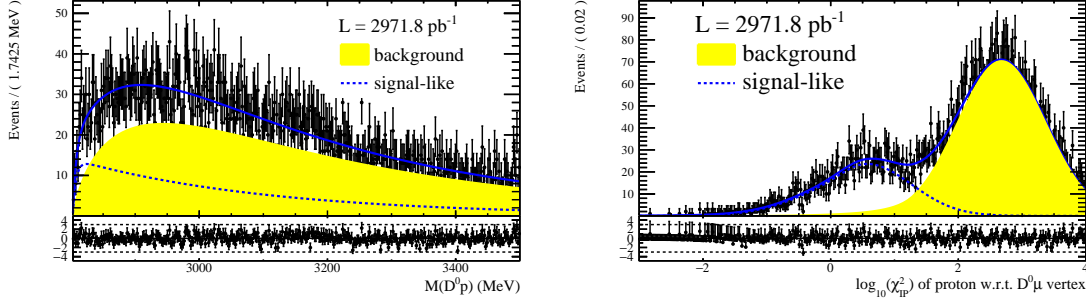


Figure 6.9: Invariant mass (left) and $\log \chi_{\text{IP}}^2$ (right) distribution for "wrong sign" (WS) candidates.

6.5 Extraction of $\Lambda_b^0 \rightarrow D^0 p \mu^- \bar{\nu}_\mu X$ signal yield together with $\Lambda_c(2880)^+$ and $\Lambda_c(2940)^+$ properties

From the previous fits different results can be obtained. Concerning the 2Dfit (see tab. 6.4 the yields for the components nonresonant signal, $\Lambda_c(2880)^+$, $\Lambda_c(2940)^+$ and enhancement are summed up to get the total $\Lambda_b^0 \rightarrow D^0 p \mu^- \bar{\nu}_\mu X$ signal yield N_{D^0p} for the calculation of \mathcal{R} . The number is

$$N_{D^0p} = (2.294 \pm 0.085) \cdot 10^4.$$

From the D^0p mass spectrum it is furthermore possible to measure the masses and widths of the $\Lambda_c(2880)^+$ and $\Lambda_c(2940)^+$ resonances. In this case it isn't needed to distinguish between nonresonant signal and background. To avoid uncertainties caused by this distinction, the onedimensional fit of the D^0p mass (see tab. 6.2 is used to get the properties of the two resonances:

$$\begin{aligned} \Lambda_c(2880)^+ : \quad & m_{\Lambda_c(2880)^+} = (2881.85 \pm 0.35) \text{ MeV}, \\ & \Gamma_{\Lambda_c(2880)^+} = (8.9 \pm 1.4) \text{ MeV}, \\ \Lambda_c(2940)^+ : \quad & m_{\Lambda_c(2940)^+} = (2936.8 \pm 2.1) \text{ MeV}, \\ & \Gamma_{\Lambda_c(2940)^+} = (26.2 \pm 7.9) \text{ MeV}. \end{aligned}$$

Table 6.4: Results of the twodimensional $M(D^0 p)$ and $\log \chi^2_{\text{IP}}$ fit.

Variable	Value
Yields	
$\Lambda_c(2880)^+$ signal yield	$(1.35 \pm 0.15) \cdot 10^3$
$\Lambda_c(2940)^+$ signal yield	$(1.13 \pm 0.23) \cdot 10^3$
mass enhancement yield	$(2.38 \pm 0.44) \cdot 10^3$
nonresonant signal yield	$(1.808 \pm 0.067) \cdot 10^4$
background yield	$(9.42 \pm 0.14) \cdot 10^3$
$\Lambda_c(2880)^+$ resonance	
mean	$(2.88185 \pm 0.00034) \cdot 10^3$
width	$(8.8 \pm 1.3) \cdot 10^0$
$\Lambda_c(2940)^+$ resonance	
mean	$(2.9367 \pm 0.0017) \cdot 10^3$
width	$(2.7 \pm 0.5) \cdot 10^1$
Low mass enhancement	
mean	$(2.84017 \pm 0.00087) \cdot 10^3$
width	$(2.52 \pm 0.34) \cdot 10^1$
Nonresonant signal	
turn on mass threshold	$(2.80124 \pm 0.0006) \cdot 10^3$
turn on slope	$(-1.3 \pm 3.9) \cdot 10^{-4}$
exponential 1 slope	$(-2.36 \pm 0.12) \cdot 10^{-2}$
exponential 2 slope	$(-7.09 \pm 0.26) \cdot 10^{-3}$
fraction exponential 1	$(7.33 \pm 0.21) \cdot 10^{-1}$
Background (mass)	
Empiric BG c_1	$(-1.595 \pm 0.05) \cdot 10^1$
Empiric BG c_2	$(0.0 \pm 150000.0) \cdot 10^{-5}$
Empiric BG p_0	$(5.6 \pm 3.0) \cdot 10^{-2}$
Signal ($\log \chi^2_{\text{IP}}$)	
mean	$(4.8 \pm 0.16) \cdot 10^{-1}$
left width 1	$(9.76 \pm 0.28) \cdot 10^{-1}$
right width 1	$(6.23 \pm 0.33) \cdot 10^{-1}$
left width 2	$(5.38 \pm 0.25) \cdot 10^{-1}$
right width 2	$(3.41 \pm 0.15) \cdot 10^{-1}$
fraction BfG 1	$(4.2 \pm 0.45) \cdot 10^{-1}$
Background ($\log \chi^2_{\text{IP}}$)	
CB mean	$(2.573 \pm 0.012) \cdot 10^0$
CB σ	$(6.86 \pm 0.11) \cdot 10^{-1}$
CB α	$(6.5 \pm 4.0) \cdot 10^0$
CB n	$(2.6 \pm 1.6) \cdot 10^0$

7 Normalisation fit

This chapter describes the analysis of the normalisation channel $\Lambda_b^0 \rightarrow \Lambda_c^+ \mu^- \bar{\nu}_\mu$ ($\Lambda_c^+ \rightarrow pK^-\pi^+$) resulting in the signal yield $N_{\Lambda_c^+}$ for the calculation of \mathcal{R} . The method is different to the one in the signal channel $\Lambda_b^0 \rightarrow D^0 p \mu^- \bar{\nu}_\mu X$ due to several reasons: The final state particles of the subdecay $\Lambda_c^+ \rightarrow pK^-\pi^+$ are all reconstructed. It is thus possible to see a clear Λ_c^+ mass peak as shown in figure 7.1. The small sidebands indicate a small combinatorial background concerning the subdecay $\Lambda_c^+ \rightarrow pK^-\pi^+$. Background coming from a random combination of a Λ_c^+ with a muon can be estimated by a look at the WS final states combinations $\Lambda_c^+ \mu^+$. Since a Λ_b^0 can't decay into a $\Lambda_c^+ \mu^+$ due to charge conservation, this unphysical combination gives a good hint for randomly combined $\Lambda_c^+ \mu^-$. The second reason why a different method is chosen compared to the $\Lambda_b^0 \rightarrow D^0 p \mu^- \bar{\nu}_\mu X$ channel is the fact that the Λ_b^0 can decay in several excited Λ_c^+ states (in the following denoted as Λ_c^{*+} for any excited Λ_c^+ state). It has been shown in ?? that the $\Lambda_b^0 \rightarrow \Lambda_c^+ \mu^- \bar{\nu}_\mu$ data is saturated by the decays $\Lambda_b^0 \rightarrow \Lambda_c^*(2595)^+ \mu^- \bar{\nu}_\mu$ and $\Lambda_b^0 \rightarrow \Lambda_c^*(2625)^+ \mu^- \bar{\nu}_\mu$. These excited Λ_c^{*+} instantly decay for instance in $\Lambda_c^+ \pi^+ \pi^-$. If these two pions aren't reconstructed, this decay can't be distinguished by its topology. That's why a different approach for the determination of $N_{\Lambda_c^+}$ has to be chosen. The solution of the latter problem is to fit the corrected $pK^-\pi^+ \mu^-$, i.e the visible Λ_b^0 mass. An explanation for this choice and the description of the fit is given in section 7.

7.1 Reduction and handling of backgrounds

This section describes the ways, how different sources of backgrounds are either handled or reduced.

7.1.1 Non Λ_c^+ background

As already mentioned the reconstructed $pK^-\pi^+$ mass delivers a nice peak forming the hadronically decaying Λ_c^+ nicely seen in figure 7.1. Events being outside of this peak can be explained by a random combination of proton, kaon and pion and thus not being decay remnants of the Λ_c^+ . Nonetheless there is also a certain amount of this "combinatoric" background in the peak region. It is statistically eliminated by a sideband subtraction (see section 2.4.1). As signal band the invariant $pK^-\pi^+$ masses in the range $M(pK^-\pi^+) \in [2260, 2320]$ MeV are chosen. The background bands are $M(pK^-\pi^+) \in [2225, 2260]$ MeV or $M(pK^-\pi^+) \in [2320, 2345]$ MeV.

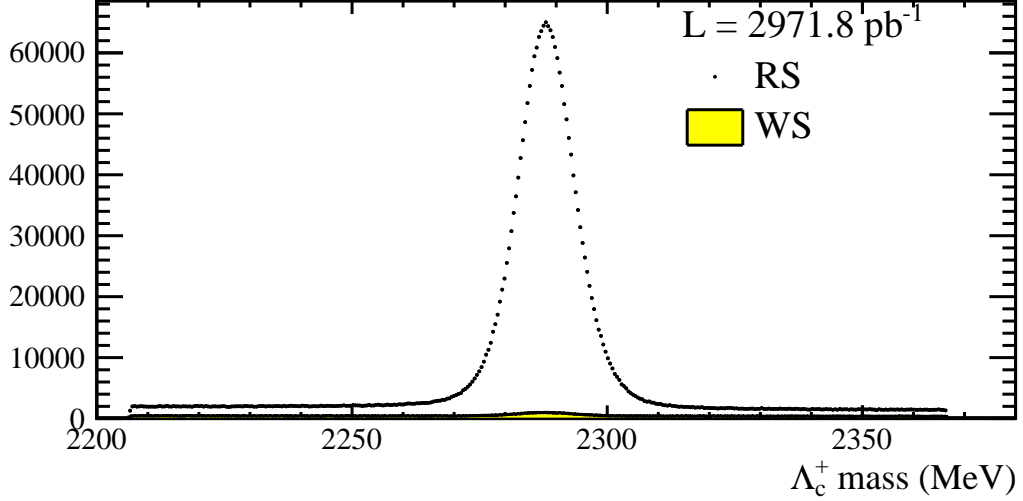


Figure 7.1: Plot of the invariant $pK^-\pi^+$ mass. A clear mass peak identified as the Λ_c^+ can be seen. The yellow shaded area shows events with the WS combination $\Lambda_c^+\mu^+$.

7.1.2 Random combinations of Λ_c^+ and μ^-

The next possible source of backgrounds are random combinations of Λ_c^+ and μ^- . Due to the semileptonic decay $\Lambda_b^0 \rightarrow \Lambda_c^+\mu^-\bar{\nu}_\mu$ and hence the missing neutrino $\bar{\nu}_\mu$ it is not possible to use a sideband subtraction on the invariant $pK^-\pi^+\mu^-$ ($\Lambda_c^+\mu^-$) mass. Thus, wrong sign (WS) events, i.e. “unphysical” events with a $\Lambda_c^+\mu^+$ in the final state as explained above are used to estimate the amount of random $\Lambda_c^+\mu^-$ background. While trying to perform the final fit later (see sec. 7.2) it turns out, that the number of WS events is too small that the fit is sensitive to it. As a consequence it is assumed that the shape and the number of the WS events are equal to the shape and number of random $\Lambda_c^+\mu^-$ combinations. Finally, the WS events are subtracted from the “right sign” (RS) events to eliminate this source of backgrounds.

7.1.3 Peaking backgrounds

The third source of backgrounds is peaking background from partially reconstructed decays. In this case the data is saturated by the decays $\Lambda_b^0 \rightarrow \Lambda_c^*(2595)^+\mu^-\bar{\nu}_\mu$ and $\Lambda_b^0 \rightarrow \Lambda_c^*(2625)^+\mu^-\bar{\nu}_\mu$ [9]. The Λ_c^{*+} subsequently decay in a Λ_c^+ and an untracked neutral remnant, e.g. π^0 , $\pi^+\pi^-$. Since this decay happens instantly it looks the same as $\Lambda_c^+ \rightarrow pK^-\pi^+$ in the detector. The solution is to fit the corrected $pK^-\pi^+\mu^-$ (alias the visible Λ_b^0) mass. A property of the corrected mass is that if the only missing particle is a massless, then the corrected mass should peak around the real mass of the mother particle, here the Λ_b^0 . If there are additionally more missing, but massive particles then this peak should be shifted to lower masses. It is thus expected that

the corrected $pK^-\pi^+\mu^-$ mass distributions look different for the semileptonic Λ_b^0 decays into a Λ_c^+ , $\Lambda_c^*(2595)^+$ and $\Lambda_c^*(2625)^+$. A fit of the corrected mass should also be able to distinguish between those components.

7.2 Fit of the $pK^-\pi^+\mu^-$ corrected mass

Having read the previous sections it should be clear, why the corrected $pK^-\pi^+\mu^-$ mass is used for the determination of $N_{\Lambda_c^+}$, the $\Lambda_b^0 \rightarrow \Lambda_c^+ \mu^- \bar{\nu}_\mu$ signal yield. Nonetheless it should be verified, that the corrected $pK^-\pi^+\mu^-$ mass is an appropriate variable. Therefore simulations for the different components, $\Lambda_b^0 \rightarrow \Lambda_c^+ \mu^- \bar{\nu}_\mu$, $\Lambda_b^0 \rightarrow \Lambda_c^*(2595)^+ \mu^- \bar{\nu}_\mu$ and $\Lambda_b^0 \rightarrow \Lambda_c^*(2625)^+ \mu^- \bar{\nu}_\mu$ are used to compare their corrected $pK^-\pi^+\mu^-$ mass shapes.

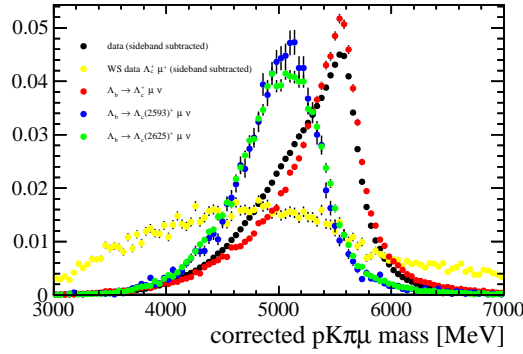


Figure 7.2: Comparison of the $pK^-\pi^+\mu^-$ corrected mass for the semileptonic Λ_b^0 decays via Λ_c^+ , $\Lambda_c^*(2593)^+$ and $\Lambda_c^*(2625)^+$ gained from simulation. The black points show the sideband subtracted data distribution. The shape of combinatorial $\Lambda_c^+ \mu^-$ background (WS events) is shown in yellow.

From figure 7.2 one can draw the following conclusions:

- The corrected $pK^-\pi^+\mu^-$ mass indeed looks different for Λ_c^+ and Λ_c^{*+} channels.
- It is not possible to distinguish between the $\Lambda_c^*(2595)^+$ and $\Lambda_c^*(2625)^+$ as their shapes are too similar.

The latter conclusion isn't really a problem since the only result of interest is the $\Lambda_b^0 \rightarrow \Lambda_c^+ \mu^- \bar{\nu}_\mu$ signal yield. A distinction among the excited states isn't needed. In the fit there will be just a component for both final states. Having these in mind, the fit procedure is done as follows:

1. The data is subtracted by the $pK^-\pi^+$ (i.e. Λ_c^+) mass bands.
2. The corrected $pK^-\pi^+\mu^-$ mass distribution is subtracted by the WS events' distribution.

3. A fit of the $pK^-\pi^+\mu^-$ mass is performed using the Beeston-Barlow method (see sec. 2.4.4) to account for uncertainties in the MC corrected mass templates. The fitted components are the Λ_c^+ signal yield and one for both excited Λ_c^{*+} channels.
4. For the plotting (see fig. 7.3 and a better comparison the WS component is added again).

The results can be seen in figure 7.3 and table 7.1. The $\Lambda_b^0 \rightarrow \Lambda_c^+ \mu^- \bar{\nu}_\mu$ signal yield $N_{\Lambda_c^+}$, required for the determination of \mathcal{R} is:

$$N_{\Lambda_c^+} = (1.5837 \pm 0.0098) \cdot 10^6$$

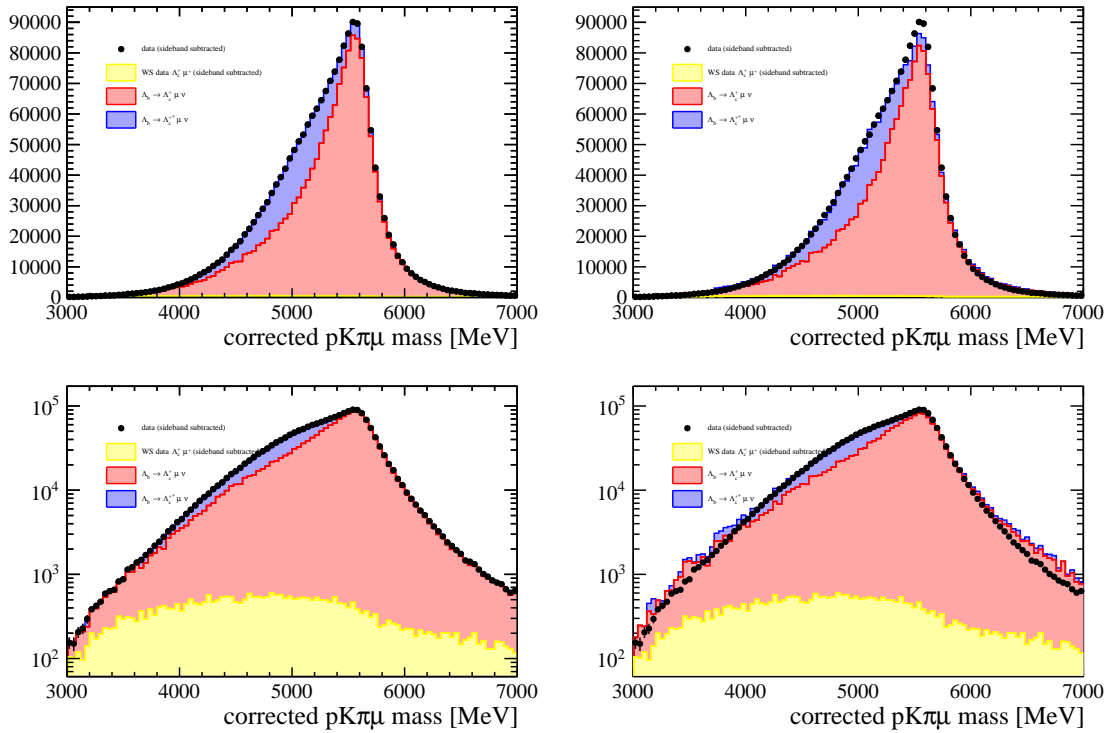


Figure 7.3: Fit to the $pK^-\pi^+\mu^-$ corrected mass for the determination of the $\Lambda_b^0 \rightarrow \Lambda_c^+ \mu^- \bar{\nu}_\mu$ signal yield. The left plot shows the fit result with the Beeston-Barlow adjusted templates, the right one the bare templates without any modification. The top row shows the result on a linear, the bottom row on logarithmic scale.

Table 7.1: Results of the Λ_c^+ corrected mass fit.

Variable	Value
Λ_c^+ candidates $N_{\Lambda_c^+}$	$(1.5837 \pm 0.0098) \cdot 10^6$
excited Λ_c^{*+} candidates	$(3.849 \pm 0.087) \cdot 10^5$
combinatoric background	$(3.406 \pm 0.026) \cdot 10^4$

8 Efficiencies

The detection and reconstruction of particle decays is not perfect at all, i.e. not all particles and tracks happening in succession of a pp interaction are detected and recorded. This discrepancy between the measured signal yields and the actually happened decays is summarized with the term “efficiencies”. There are several reasons why different kinds of efficiencies occur. Here are some examples:

- Particles are flying out of the detector.
- A particle traverses a sensor in the deadtime, i.e. a signal caused by an earlier particle is still processed. In this time, the sensor isn’t able to process the second signal.
- Applying cuts for the reduction of background prevents signal events to pass these cuts as well
- ...

It’s obvious that this list above is only the tip of the iceberg. Nonetheless it’s crucial to account for these efficiencies if one measures a physical quantity reliant on the number of events. The way how the efficiencies for the $\Lambda_b^0 \rightarrow D^0 p \mu^- \bar{\nu}_\mu X$ and $\Lambda_b^0 \rightarrow \Lambda_c^+ \mu^- \bar{\nu}_\mu$ enter the measurement of the relative branching ratio \mathcal{R} is shown in equation (4.1).

The determination of the efficiencies requires the use of simulations. These simulation samples contain informations about all generated events as well as reconstructed events after the simulation of the detector. The naive way would be to divide the number of reconstructed MC events after applying all selection cuts and divide this by the number of generated events. This efficiency is hereafter called selection efficiency ϵ_{sel} . Nonetheless, the generation of the events isn’t efficient at all. Several requirements are already applied during generation to reduce the computation time of the simulation production. Above all the simulation of the detector takes a lot of time. That’s why all generated events are required to be in the LHCb acceptance. A further acceleration of the production process can be achieved with additional requirements on the final state particles’ (transverse) momenta. Concerning the $\Lambda_b^0 \rightarrow D^0 p \mu^- \bar{\nu}_\mu X$ and $\Lambda_b^0 \rightarrow \Lambda_c^+ \mu^- \bar{\nu}_\mu$ channel these requirements are different and likewise the efficiencies of the generation process. Thus, the so called generator level efficiency ϵ_{gen} also has to be determined for both channels. The total efficiency used for the calculation of \mathcal{R} is then the product $\epsilon_{\text{gen}} \cdot \epsilon_{\text{sel}}$.

As life is not that easy the simulations don’t perfectly describe the data. Above all the $\Lambda_b^0 \rightarrow D^0 p \mu^- \bar{\nu}_\mu X$ signal simulation doesn’t contain a proper physics description

and is thus in disagreement with data. Unfortunately, no theory prediction of the $\Lambda_b^0 \rightarrow D^0 p \mu^- \bar{\nu}_\mu X$ channel is available to fix this problem. The plots in figure 8.1 show a comparison of data (black points) and the simulation (red lines). To get a better description of the decay the simulation hence has to be reweighted. This should lead to a more proper estimate of the efficiency. Several reweighting steps are applied and will be described in the following.

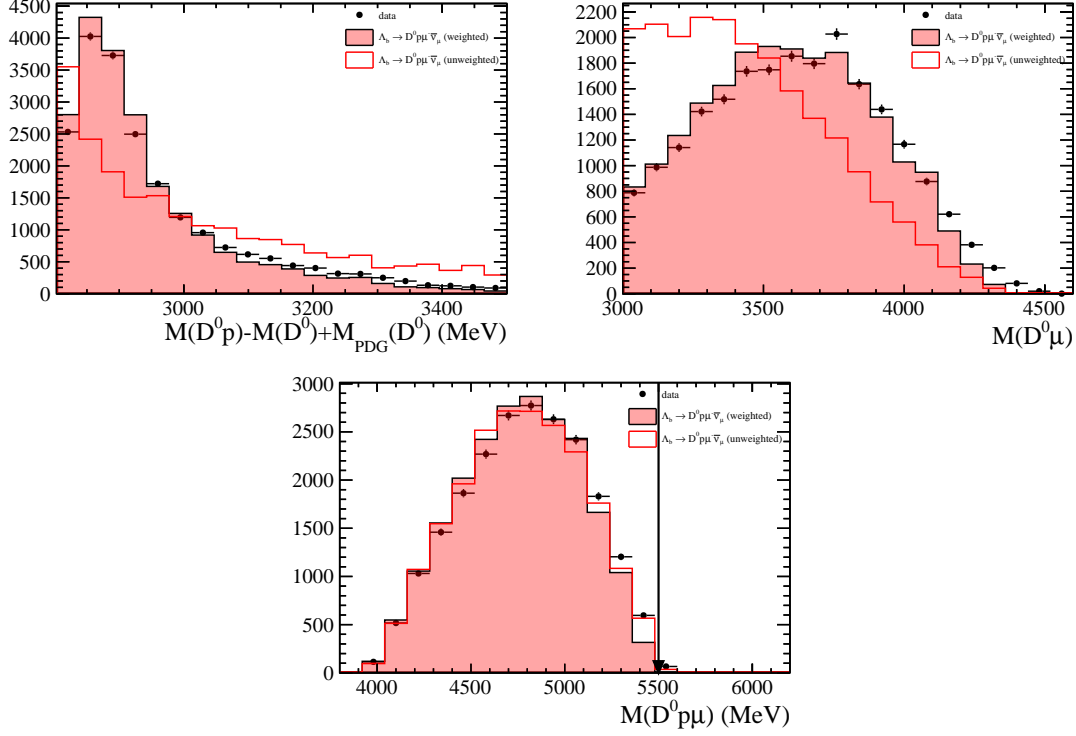


Figure 8.1: Comparison of data (black points) and simulation for the $\Lambda_b^0 \rightarrow D^0 p \mu^- \bar{\nu}_\mu X$ channel before (red line) and after (red shaded area) three-dimensional reweighting as described in the text (see sec. 8.2).

8.1 Kinematic reweighting of the $\Lambda_b^0 \rightarrow D^0 p \mu^- \bar{\nu}_\mu X$ and $\Lambda_b^0 \rightarrow \Lambda_c^+ \mu^- \bar{\nu}_\mu$ channel

The production of Λ_b^0 baryons depends strongly on their transverse momentum as figure 8.2 (left) from ref. [10] shows. This dependence isn't well emulated in the simulation and has thus to be corrected. This was already done in the semileptonic LHCb-measurement of $|V_{ub}|$ in ref. [9] using the decay $\Lambda_b^0 \rightarrow J/\psi D^0 p$. To calculate the weights they compared data and simulation of this hadronic Λ_b^0 decay channel, shown in figure 8.2 (right). In this analysis, the used weights are determined from the same channel with the help figure 8.2 (right). The reweighting is applied in both,

$\Lambda_b^0 \rightarrow D^0 p \mu^- \bar{\nu}_\mu X$ and $\Lambda_b^0 \rightarrow \Lambda_c^+ \mu^- \bar{\nu}_\mu$, channels according to the true Λ_b^0 transverse momentum p_T , i.e. the actual generated transverse momentum.

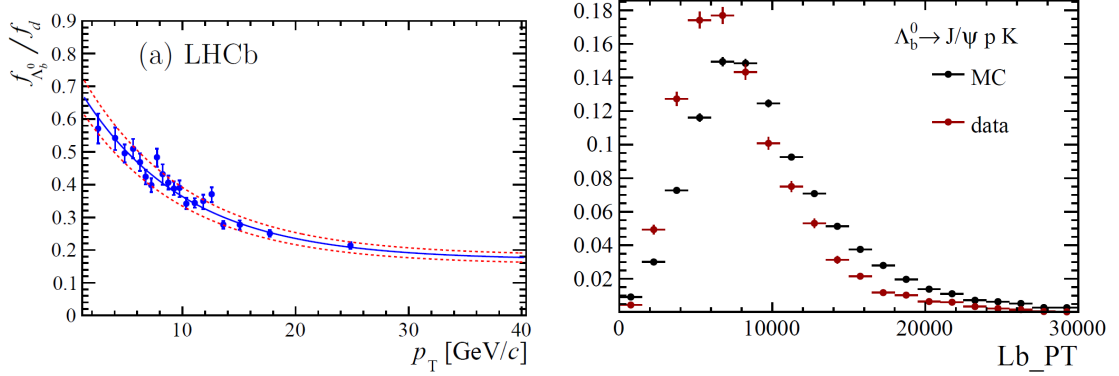


Figure 8.2: Left: Ratio of Λ_b^0 to B^0 production as a function of p_T . Figure taken from [10]. Right: Transverse Λ_b^0 momentum for $\Lambda_b^0 \rightarrow J/\psi D^0 p$ decays in data and simulation. Figure taken from the documentation belonging to [9].

8.2 Reweighting of the $\Lambda_b^0 \rightarrow D^0 p \mu^- \bar{\nu}_\mu X$ decay simulation

It has already been mentioned that the underlying physics in the $\Lambda_b^0 \rightarrow D^0 p \mu^- \bar{\nu}_\mu X$ simulation is wrong. Since there aren't any theoretical predictions on that channel, the reweighting of the simulation has to be done carefully. To come as close to data as possible, a three-dimensional reweighting in the variables

- $M(D^0 p)$
- $M(D^0 \mu^-)$
- $M(D^0 p \mu^-)$

has been chosen. This choice is not trivial and above all obvious, but there are several reasons for it:

1. The simulation is completely off from the data distribution in these variables.
2. These variables are already available at generator level, i.e. before the detector response is simulated. To calculate the selection efficiency the simulation has to be reweighted at generator stage as well.

3. There aren't any selection requirements on these variables. Otherwise, no weights could be assigned to ones not fulfilling the requirements at generator level ¹.

After the description of the reweighting and efficiency calculation process, it should become clear why these three points are important:

- **Determination of the weights**

There are two normalized threedimensional histograms drawn for both, generated events (in the following called MCDecayTreeTuple or MCDTT) and events after reconstruction, applying selection cuts and the kinematic reweighting (DecayTreeTuple or DTT). Both histograms have the three variables mentioned above on their axes. The histogram with the weights is now calculated by dividing the DTT histogram through the MCDTT histogram.

- **Assigning weights to the events**

Now, this weight histogram is used to assign a weight to each DTT (w_{DTT}) and MCDTT (w_{MCDTT}) event. To get the correct bin in the weight histogram the generated masses $M_{\text{true}}(D^0 p)$, $M_{\text{true}}(D^0 \mu^-)$ and $M_{\text{true}}(D^0 p \mu^-)$ are used.

- **Calculation of the efficiency**

The efficiency can now be calculated with

$$\epsilon = \frac{\sum w_{\text{DTT}}}{\sum w_{\text{MCDTT}}}, \quad (8.1)$$

To account for the loss of statistical power due to reweighting, both numerator and denominator in equation (8.1) are multiplied by the renormalisation factor $\sum w_{\text{MCDTT}} / \sum w_{\text{DTT}}^2$. This doesn't affect the central value of ϵ but influences the statistical error, which is calculated using binomial statistics.

It should now be clear, that with this procedure one must not cut on the weighting variables, since otherwise the weights outside the cut region would be zero. Hence it wouldn't be clear which weights have to be assigned to the MCDTT events. The distribution of the masses after reweighting are also shown in figure 8.1. A decided improvement of the data description can be figured out. Many more comparisons between data and simulation before and after reweighting can be found in the appendix B in figure B.1. Having these reweighting steps in mind, it is now possible to calculate the efficiencies at different stages.

8.3 Generator level efficiencies

As a reminder, generator level efficiencies arise due to the fact, that one demands the generated events to be in the LHCb acceptance and apply some (loose) requirements

¹There exists a selection requirement on $M(D^0 p \mu^-)$ in this analysis to eliminate $\Lambda_b^0 \rightarrow D^0 p \pi^-$ background, but less than 0.5% of all events have their generated mass above this value. Thus, its impact on the efficiency can be neglected.

on the kinematics to accelerate the simulation process. The generator level samples are reweighted as described above: the $\Lambda_b^0 \rightarrow \Lambda_c^+ \mu^- \bar{\nu}_\mu$ sample with the kinematic p_T (Λ_b^0) reweighting and the $\Lambda_b^0 \rightarrow D^0 p \mu^- \bar{\nu}_\mu$ sample with both reweightings. For signal and normalization channel the following generator level efficiencies are obtained:

$$\begin{aligned}\epsilon_{\text{gen}, \Lambda_c^+} &= 0.345 \pm 0.016, \\ \epsilon_{\text{gen}, D^0 p} &= 0.228 \pm 0.058.\end{aligned}$$

8.4 Reconstruction and selection efficiencies

The reconstruction and selection efficiencies are calculated analogously. The same reweighting procedure on the different samples is performed. The results for signal and normalization channel are:

$$\begin{aligned}\epsilon_{\text{sel}, \Lambda_c^+} &= (3.921 \pm 0.023) \times 10^{-3}, \\ \epsilon_{\text{sel}, D^0 p} &= (4.85 \pm 0.16) \times 10^{-3}.\end{aligned}$$

8.5 Total efficiencies

To summarise the values above the total efficiencies for the channels are:

$$\begin{aligned}\epsilon_{D^0 p} &= \epsilon_{\text{gen}, D^0 p} \cdot \epsilon_{\text{sel}, D^0 p} = (1.10 \pm 0.28) \times 10^{-3}, \\ \epsilon_{\Lambda_c^+} &= \epsilon_{\text{gen}, \Lambda_c^+} \cdot \epsilon_{\text{sel}, \Lambda_c^+} = (1.352 \pm 0.065) \times 10^{-3}.\end{aligned}$$

For the consideration of systematics later it is sometimes more useful to consider the ratio of both efficiencies

$$\frac{\epsilon_{\Lambda_c^+}}{\epsilon_{D^0 p}} = 1.22 \pm 0.32.$$

9 Backgrounds

The big disadvantage of semileptonic decays is that the neutrino can't be reconstructed. At hadron colliders like the LHC it is impossible to know the initial state, so one doesn't have enough constraints to reconstruct the full kinematic information about the decaying particle. Being aware of these problems due to experimental setup it is clear that one can't use a well reconstructed Λ_b^0 mass peak to separate signal from background. A main source of background is expected to be the decay $B^0/B^+ \rightarrow D^0 \mu^- \bar{\nu}_\mu X$ where one randomly combines a proton to this decay. This background is handled by the fit of the $\log \chi_{\text{IP}}^2$ distribution. Other sources of backgrounds and their possible impact on the obtained signal yield $N_{D^0 p}$ are discussed in the following. For the $\Lambda_b^0 \rightarrow \Lambda_c^+ \mu^- \bar{\nu}_\mu$ channel it is assumed, that all non-negligible backgrounds are accounted for due to the sideband subtraction and including wrong sign events as well as resonant modes components in the fit. The discussion in this chapter thus refers completely to the $\Lambda_b^0 \rightarrow D^0 p \mu^- \bar{\nu}_\mu X$ channel.

9.1 Proton misidentification

A possible source of backgrounds is that one misinterprets a decay as $\Lambda_b^0 \rightarrow D^0 p \mu^- \bar{\nu}_\mu X$ since one misidentifies a final state particle. In this analysis it is most likely that the proton is misidentified since the final state pion and kaon are reconstructed to a D^0 yielding in a nice peak and the muon leaves a clear signature in the detector due to its relatively long lifetime and low interaction with matter. Examples for these kind of backgrounds are the decays $B_s^0 \rightarrow D^0 K^+ \mu^- \bar{\nu}_\mu X$ and $B^0/B^+ \rightarrow D^0 \pi^+ \mu^- \bar{\nu}_\mu X$, where either the K^+ or π^+ is misidentified as proton. Though there are tight requirements on the proton identification at selection stage, the data will still be polluted by misidentified particles. To identify the amount of misidentified protons, a slightly different data sample than the nominal one is used. In this sample no requirements on the proton identification are applied. Except for those all other requirements are the same as described in section 5. However the removal of the particle identification requirements lets the data size of the sample rapidly increase. To keep the data size acceptable a so called 5% prescaling has been applied, i.e. only 5% of all events are actually stored. The decision if a particle is stored or not is made by random. The study on misidentified backgrounds is done in three steps.

9.1.1 Definition of PID particle regions - Number of particle candidates

As a first step we define PID regions for protons, pions and kaons in the PIDK vs. PIDp plane. The proton region is motivated by the cuts applied in the analysis. In detail these are:

- proton: $\text{PIDp} - \text{PIDK} > 10.0$ and $\text{PIDp} > 10.0$
- pion: $\text{PIDp} < 10.0$ and $\text{PIDK} < 0.0$
- kaon: $\text{PIDp} - \text{PIDK} < 10.0$ and $\text{PIDK} > 0.0$

Furthermore these regions and their population are visualised in figure 9.1. From this we get the number of candidates for each particle species, in the following denoted as N_{cand}^i , with $i \in [\pi, K, p]$. The number of candidates are

$$N_{\text{cand}}^{\pi} = 5052 \pm 71, \quad (9.1)$$

$$N_{\text{cand}}^K = 2175 \pm 47, \quad (9.2)$$

$$N_{\text{cand}}^p = 989 \pm 31 \quad (9.3)$$

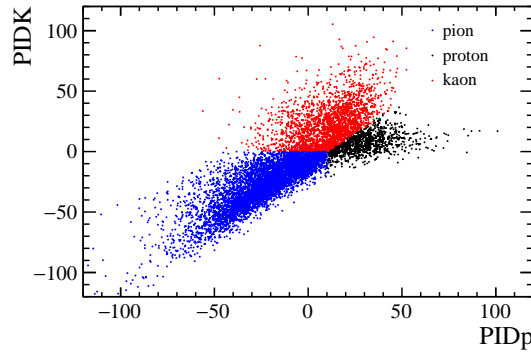


Figure 9.1: Regions for the number of particle candidates.

Determination of “true” candidates with PID efficiencies

The LHCb PIDcalib tool is used to determine the PID efficiencies, that a real proton (or kaon / pion) is identified as what we call a proton, pion or kaon according to our defined PID regions. The PID efficiency for each of the 9 combinations is determined binwise depending on the particle momentum. The results can be seen in figure 9.2.

To determine a final value for each efficiency, the histograms are weighted w.r.t. the kinematic distribution of our data sample. The result is:

$$\begin{pmatrix} \epsilon_{\pi^+ \rightarrow \pi^+} & \epsilon_{K^- \rightarrow \pi^+} & \epsilon_{p \rightarrow \pi^+} \\ \epsilon_{\pi^+ \rightarrow K^-} & \epsilon_{K^- \rightarrow K^-} & \epsilon_{p \rightarrow K^-} \\ \epsilon_{\pi^+ \rightarrow p} & \epsilon_{K^- \rightarrow p} & \epsilon_{p \rightarrow p} \end{pmatrix} = \begin{pmatrix} 0.9409 & 0.0241 & 0.1309 \\ 0.0474 & 0.9681 & 0.3798 \\ 0.0117 & 0.0077 & 0.4893 \end{pmatrix}$$

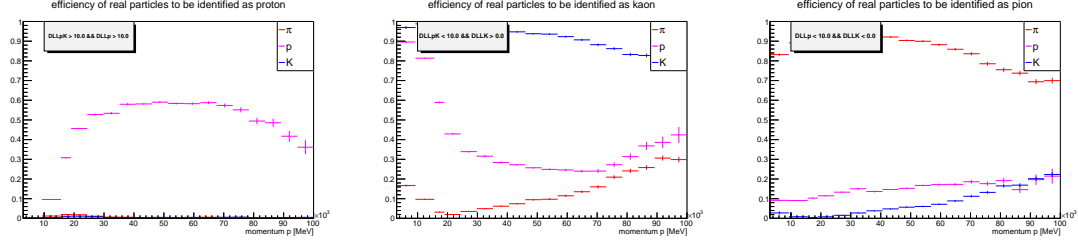


Figure 9.2: Efficiencies determined with PIDcalib.

Here, $\epsilon_{i \rightarrow j}$ denotes the efficiency, that a real particle i is identified as what we call j . For the following analysis, PID efficiency errors are assumed to be negligible compared to the corresponding uncertainties of the particle candidates N_{cand}^i . With the PID efficiencies $\epsilon_{i \rightarrow j}$ and the number of particle candidates N_{cand}^k , the number of “true” particles is determined by solving the matrix equation

$$\begin{pmatrix} N_{\text{cand}}^\pi \\ N_{\text{cand}}^K \\ N_{\text{cand}}^p \end{pmatrix} = \begin{pmatrix} \epsilon_{\pi \rightarrow \pi} & \epsilon_{K \rightarrow \pi} & \epsilon_{p \rightarrow \pi} \\ \epsilon_{\pi \rightarrow K} & \epsilon_{K \rightarrow K} & \epsilon_{p \rightarrow K} \\ \epsilon_{\pi \rightarrow p} & \epsilon_{K \rightarrow p} & \epsilon_{p \rightarrow p} \end{pmatrix} \begin{pmatrix} N_{\text{true}}^\pi \\ N_{\text{true}}^K \\ N_{\text{true}}^p \end{pmatrix},$$

which delivers

$$N_{\text{true}}^\pi = 5075 \pm 76, \quad (9.4)$$

$$N_{\text{true}}^K = 1260 \pm 55, \quad (9.5)$$

$$N_{\text{true}}^p = 1880 \pm 65 \quad (9.6)$$

Estimate of misidentified protons

Using the results of the previous subsections it is possible to estimate the number of misidentified protons (“true” kaons or pions identified as a proton) by multiplying the number of “true” particles N_{true}^i with the PID efficiency $\epsilon_{i \rightarrow p}$ to be identified as proton.

$$N^\pi = \epsilon_{\pi \rightarrow p} N_{\text{true}}^\pi = 59.25 \pm 0.89, \quad (9.7)$$

$$N^K = \epsilon_{K \rightarrow p} N_{\text{true}}^K = 9.74 \pm 0.42, \quad (9.8)$$

$$N^p = \epsilon_{p \rightarrow p} N_{\text{true}}^p = 920 \pm 32 \quad (9.9)$$

Thus, the amount of misidentified protons is at a single-digit percent level, namely $(6.98 \pm 0.24)\%$. Note that the absolute values can’t be compared to the signal yields for both channels since this background study was done with a prescaled sample and without PID cuts.

The following backgrounds to the the $\Lambda_b^0 \rightarrow D^0 p \mu \nu X$ sample are considered:

- **Prompt D^0**

The prompt D^0 cross section exceeds that of Λ_b^0 production by a factor of

Table 9.1: Estimate of the residual peaking backgrounds.

Mode	Estimated B/S	Branching fraction	Production factor	Comment
Signal ($\Lambda_b \rightarrow D^0 p \mu^- \nu$)	1	$\approx 1.5 \times 10^{-3}$	1	–
Total peaking background	5%	–	–	–
$\Lambda_b \rightarrow D^0 p \pi^-$	Zero	$(5.9^{+4.0}_{-3.2}) \times 10^{-4}$	1	Mass veto
$\Lambda_b \rightarrow D^0 p \pi(\pi\pi, \pi^0)$	5%	$\approx 10^{-3}$	1	$\pi \rightarrow \mu$ mis-ID
Prompt D^0	$< 10^{-3}$	N/A	N/A	$\log(\text{IP}, D^0)$
$B_s \rightarrow D^0 K \mu \nu X$	p -misid	$\approx 6 \times 10^{-3}$ (resonant part)	0.5	& Λ_b combination cuts p -mis-ID

twenty or so. The background from prompt charm production is typically measured to be **a few percent** in studies of semileptonic b decays. Suggest to plot the distribution of the $\log(\text{IP})$ of the D^0 , which should reveal the prompt component. This should be clearer in candidates with a wrong sign muon, or wrong sign proton, or both. By requiring a large $\log(\text{IP})$ of the D^0 , we should be able to eliminate this background altogether.

- $B_s^0 \rightarrow D^0 K \mu \nu X$

Where the kaon is mis-identified as a proton. The mis-id rate should be a few percent, given our tight proton PID requirements. And $f_{\Lambda_b}/f_s \sim 2$. We should be able to estimate this contribution quite precisely just from the numbers in an early LHCb study with 2010 data [?].

- $B^{0,+} \rightarrow D^0 \pi^+ \mu \nu X$

Where the pion is mis-identified as a proton. The mis-id rate should be very small, and these decays are quite well understood.

- $B^{0,+} \rightarrow D^0 \mu \nu X$ **plus a proton from the PV or other b**

This component is subtracted in our fit to the $\log(\text{IP})$ of the proton w.r.t. the $D^0 \mu$ vertex.

- $\Lambda_b^0 \rightarrow D^0 p \pi X$

Where the pion is mis-identified as a muon. The branching fraction of this decay has been measured to be less than 10^{-3} . It sits in a very narrow region of $D^0 p \mu^-$ invariant mass peaking at the Λ_b^0 mass. This background is eliminated by a cut on the $D^0 p \mu^-$ mass as can be seen in figure 9.3.

- $\Lambda_b^0 \rightarrow D^0 p 3\pi$

The branching fraction should be similar to $\Lambda_b^0 \rightarrow D^0 p \pi X$, i.e. of order 10^{-4} . The amount should decrease with increasing muon identification. Figure 9.4 shows a 2D plot of the $D^0 p \mu$ mass versus the particle identification variable PID_{μ} of the muon. Backgrounds coming from a Λ_b^0 decay into 3 pions should cluster at low PID_{μ} , where it is rather probable that a muon is misidentified than in the high PID_{μ} region.

- $\Lambda_b^0 \rightarrow D\Lambda_c$
This decay hasn't been measured but it should have a branching ratio of around 10^{-2} , similar to $B \rightarrow DD_s$. If the Λ_c decays to $pK\pi$, then we get another 4×10^{-2} and we need to get the muon from somewhere else, or it has to be from $K \rightarrow \mu$ mis-id. The vertex quality will be somewhat spoilt by the Λ_c flight. So this should be a sub-percent-level background. One could also get $\Lambda_c N^* \mu \nu$, where we get the muon and proton without any mis-id?
- $\Lambda_b^0 \rightarrow D^0 D^- p$
This decay hasn't been measured but it should be similar to $B \rightarrow DDK$ at a few times 10^{-3} . The inclusive $D^- \rightarrow \mu^- X$ branching fraction is about 10^{-2} . This should still be a percent level background.
- **prompt $\Lambda_c(2880)^+$ or $\Lambda_c(2940)^+$ decay with an μ^- from somewhere else**
This background should be reduced by requiring the $\Lambda_c(2880)^+$ resp. $\Lambda_c(2940)^+$ vertex to be well separated from the PV.
- $\Sigma_b \rightarrow \Lambda_b^0 \pi$, where the pion isn't reconstructed.

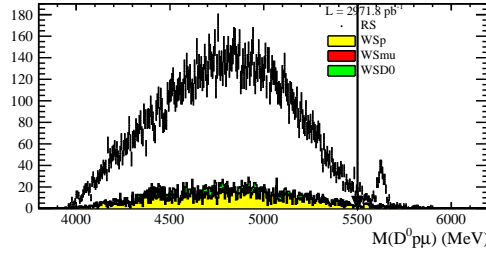


Figure 9.3: Invariant $D^0 p \mu^-$ mass. The arrow indicates the cut applied in this analysis. The peak at Λ_b^0 mass (≈ 5620 MeV) comes from the decay $\Lambda_b^0 \rightarrow D^0 p \pi$ where the pion is misidentified as muon.

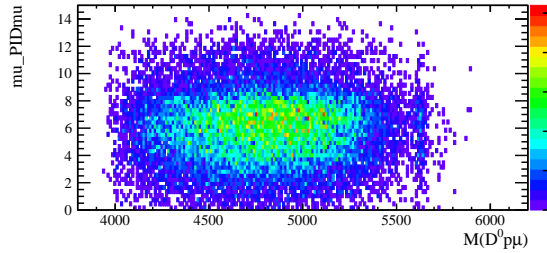


Figure 9.4: Invariant $D^0 p \mu^-$ mass versus PIDmu of the muon. No structures tending to low PIDmu can be seen.

10 Systematics

A Massresolution

Figure A.1 shows the fits to all bins of D^0p mass for the determination of the massresolution. The whole method and prodecure is described in section 6.2.

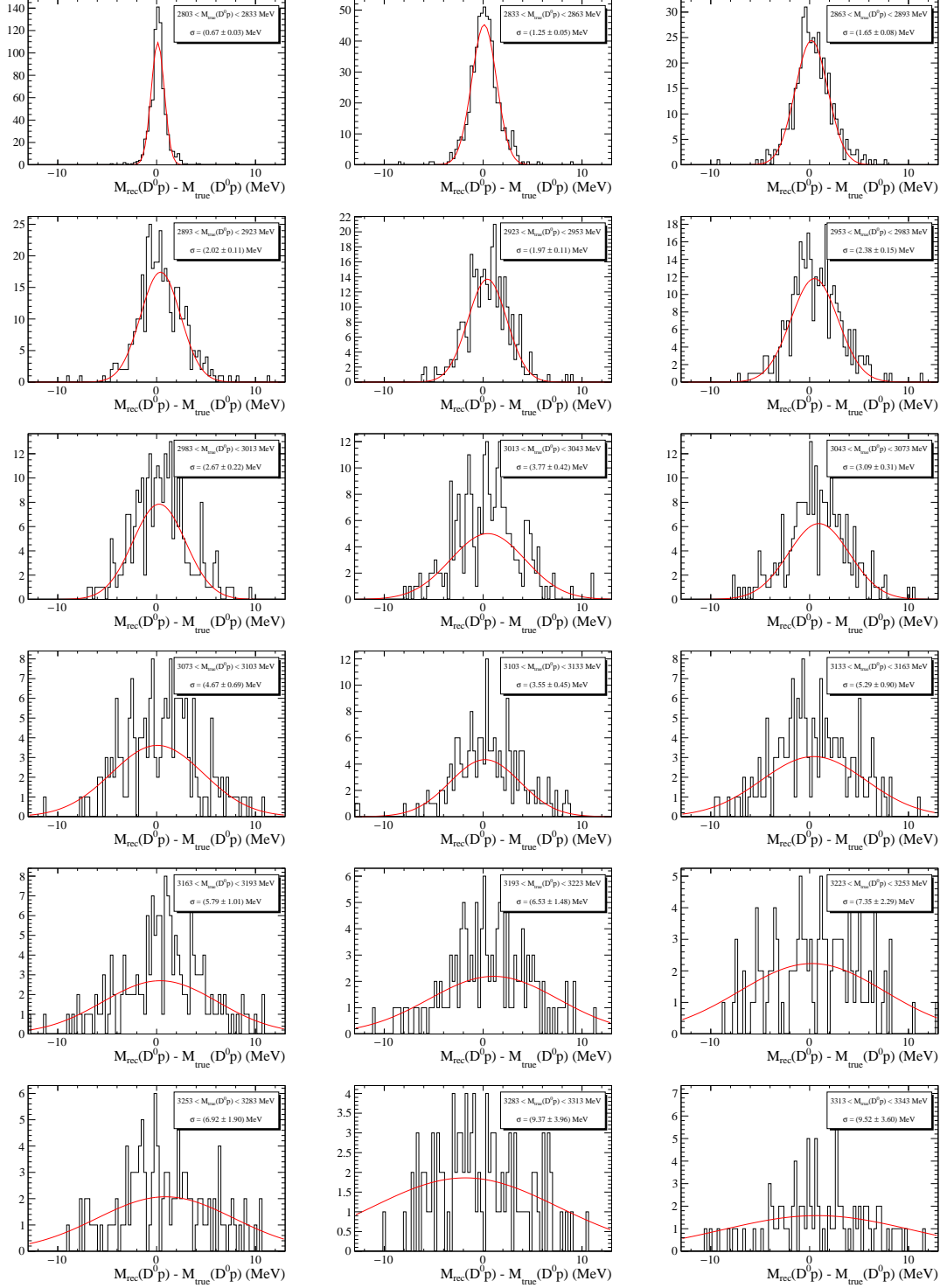


Figure A.1: Fit of a Gaussian to the difference between generated and reconstructed $D^0 p$ mass (simulation sample) in bins of 30 MeV $D^0 p$ mass (first 18 bins of 24 shown here). The width of the Gaussian is taken as mass resolution for the respective bin.

B Reweighting of $\Lambda_b^0 \rightarrow D^0 p \mu^- \bar{\nu}_\mu X$ decay simulation

Figure B.1 shows several more comparisons of data and simulation before and after reweighting. More on the reweighting process can be found in section 8.2.

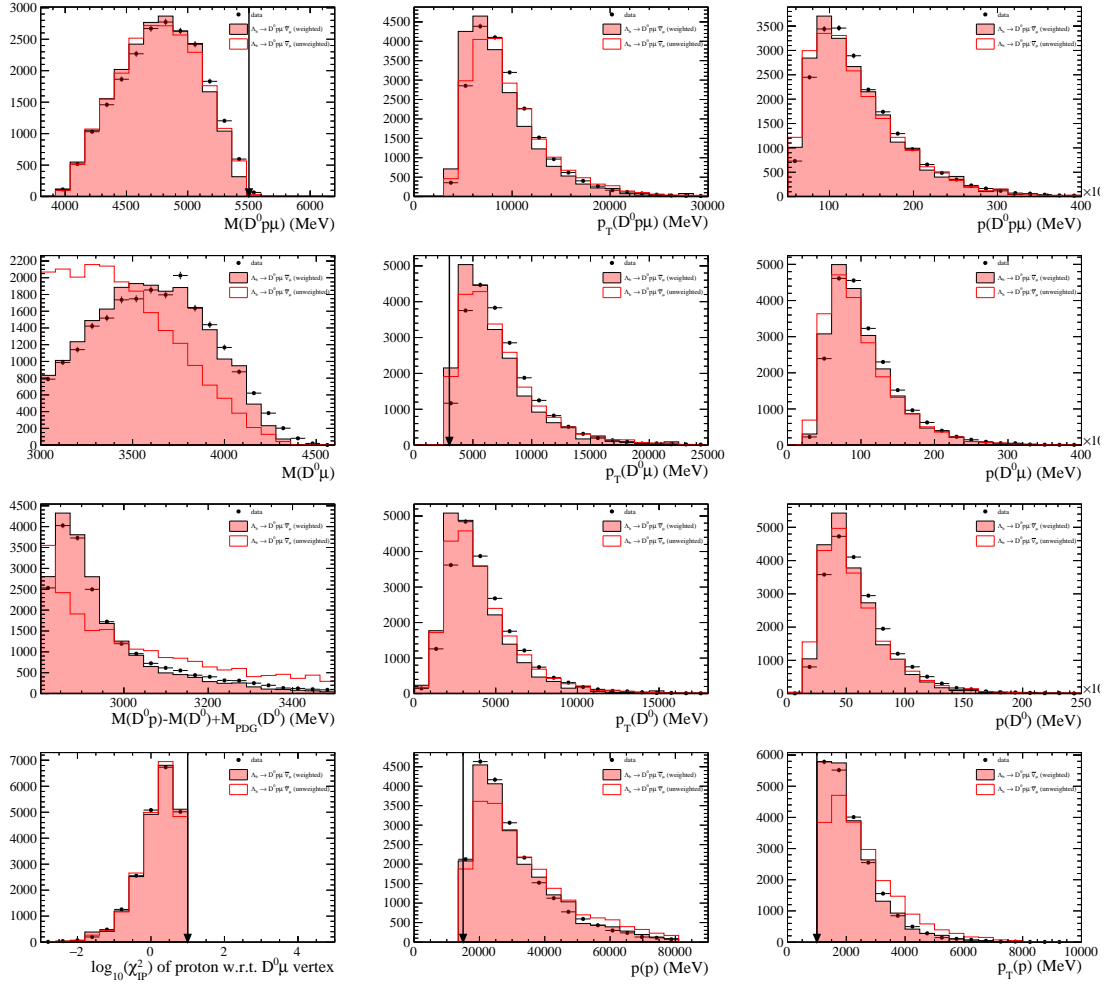


Figure B.1: Comparison of data (black points) and simulation for the $\Lambda_b^0 \rightarrow D^0 p \mu^- \bar{\nu}_\mu X$ channel before (red line) and after (red shaded area) three-dimensional reweighting as described in the text (see sec. 8.2).

List of Figures

3.1	The LHCb detector.	8
3.2	Schematic representation of an R and a Φ sensor. The R sensor strips are arranged into four approximately 45° segments and have routing lines perpendicular to the strips. The Φ sensor has two zones with inner and outer strips. The routing lines of the inner strips are orientated parallel to the outer strips. Figure and caption taken from [4].	10
3.3	Cross section in the (x, z) plane of the VELO silicon sensors, at $y = 0$, with the detector in the fully closed position. The front face of the first modules is also illustrated in both the closed and open positions. The two pile-up veto stations are located upstream of the VELO sensors. Figure and caption taken from [1].	10
3.4	Layout of the Tracker Turicensis (TT). Figure taken from [5].	11
3.5	Layout of a x detection layer in the second Inner Tracker (IT) station. Figure taken from [1].	12
6.1	Fit to the $\log \chi_{\text{IP}}^2$ distribution of the signal simulation. As parametrization a double Bifurcated Gaussian has been chosen.	17
6.2	Comparison of RS and WS events in the background MC. Both, RS and WS shapes are very similar and can thus be added to increase statistics.	17
6.3	Fit to the (RS and WS added) $\log \chi_{\text{IP}}^2$ shape of the background simulation.	18
6.4	Fit to the $\log \chi_{\text{IP}}^2$ distribution of the data sample.	19
6.5	Fit to $D^0 p$ mass of WS proton events.	20
6.6	1D fit of the $D^0 p$ mass distribution for $\log \chi_{\text{IP}}^2 < 1$. The left side shows a fit with two resonances and a nonresonant part. Different attempts have been made to get a proper and converging fit. This issue can be solved by adding an additional component (right figure, green line), here parametrized like the two resonances.	21
6.7	Left: Fit of a Gaussian to the difference between generated and reconstructed $D^0 p$ mass (simulation sample) in the range $2863 < M(D^0 p) < 2893$ MeV. The width of the Gaussian is taken as mass-resolution. Right: Obtained massresolutions for all bins. The large errors in the higher bins doesn't matter for the desired purpose as only the bins containing the resonances are relevant.	23

6.8	Twodimensional fit on the $\Lambda_b^0 \rightarrow D^0 p \mu^- \bar{\nu}_\mu X$ candidates. There are shown the $D^0 p$ mass (top) and $\log \chi_{\text{IP}}^2$ (bottom) projection. The total fit parametrization is summarized in table 6.3.	24
6.9	Invariant mass (left) and $\log \chi_{\text{IP}}^2$ (right) distribution for “wrong sign” (WS) candidates.	25
7.1	Plot of the invariant $pK^-\pi^+$ mass. A clear mass peak identified as the Λ_c^+ can be seen. The yellow shaded area shows events with the WS combination $\Lambda_c^+ \mu^+$	28
7.2	Comparison of the $pK^-\pi^+\mu^-$ corrected mass for the semileptonic Λ_b^0 decays via Λ_c^+ , $\Lambda_c^*(2593)^+$ and $\Lambda_c^*(2625)^+$ gained from simulation. The black points show the sideband subtracted data distribution. The shape of combinatorial $\Lambda_c^+ \mu^-$ background (WS events) is shown in yellow.	29
7.3	Fit to the $pK^-\pi^+\mu^-$ corrected mass for the determination of the $\Lambda_b^0 \rightarrow \Lambda_c^+ \mu^- \bar{\nu}_\mu$ signal yield. The left plot shows the fitresult with the Beeston-Barlow adjusted templates, the right one the bare templates without any modification. The top row shows the result on a linear, the bottom row on logarithmic scale.	30
8.1	Comparison of data (black points) and simulation for the $\Lambda_b^0 \rightarrow D^0 p \mu^- \bar{\nu}_\mu X$ channel before (red line) and after (red shaded area) threedimensional reweighting as described in the text (see sec. 8.2).	33
8.2	Left: Ratio of Λ_b^0 to B^0 production as a function of p_T . Figure taken from [10]. Right: Transverse Λ_b^0 momentum for $\Lambda_b^0 \rightarrow J/\psi D^0 p$ decays in data and simulation. Figure taken from the documentation belonging to [9].	34
9.1	Regions for the number of particle candidates.	38
9.2	Efficiencies determined with PIDcalib.	39
9.3	Invariant $D^0 p \mu^-$ mass. The arrow indicates the cut applied in this analysis. The peak at Λ_b^0 mass (≈ 5620 MeV) comes from the decay $\Lambda_b^0 \rightarrow D^0 p \pi$ where the pion is misidentified as muon.	41
9.4	Invariant $D^0 p \mu^-$ mass versus PIDmu of the muon. No structures tending to low PIDmu can be seen.	41
A.1	Fit of a Gaussian to the difference between generated and reconstructed $D^0 p$ mass (simulation sample) in bins of 30 MeV $D^0 p$ mass (first 18 bins of 24 shown here). The width of the Gaussian is taken as massresolution for the respective bin.	44
B.1	Comparison of data (black points) and simulation for the $\Lambda_b^0 \rightarrow D^0 p \mu^- \bar{\nu}_\mu X$ channel before (red line) and after (red shaded area) threedimensional reweighting as described in the text (see sec. 8.2).	45

List of Tables

6.1	Results of the onedimensional $\log \chi^2_{\text{IP}}$ fit on data.	18
6.2	Results of the $D^0 p$ mass fit.	22
6.3	Summary of the parameterization of the 2D fit	23
6.4	Results of the twodimensional $M(D^0 p)$ and $\log \chi^2_{\text{IP}}$ fit.	26
7.1	Results of the Λ_c^+ corrected mass fit.	31
9.1	Estimate of the residual peaking backgrounds.	40

Bibliography

- [1] LHCb collaboration, A. A. Alves Jr. *et al.*, *The LHCb detector at the LHC*, JINST **3** (2008) S08005.
- [2] LHCb Collaboration, *LHCb VELO (VERtex LOCator): Technical Design Report*, Technical Design Report LHCb, CERN, Geneva, 2001.
- [3] LHCb, R. Aaij *et al.*, *Precision measurement of the B_s^0 - \bar{B}_s^0 oscillation frequency with the decay $B_s^0 \rightarrow D_s^- \pi^+$* , New J. Phys. **15** (2013) 053021, [arXiv:1304.4741](#).
- [4] R. Aaij *et al.*, *Performance of the LHCb Vertex Locator*, JINST **9** (2014) 09007, [arXiv:1405.7808](#).
- [5] LHCb Silicon Tracker Group, J. Luisier, *Performance of LHCb Silicon Tracker Detector in the LHC*, Phys. Procedia **37** (2012) 851.
- [6] S. Tolk, J. Albrecht, F. Dettori, and A. Pellegrino, *Data driven trigger efficiency determination at LHCb*, Tech. Rep. LHCb-PUB-2014-039. CERN-LHCb-PUB-2014-039, CERN, Geneva, May, 2014.
- [7] BaBar, B. Aubert *et al.*, *Observation of a charmed baryon decaying to $D^0 p$ at a mass near $2.94\text{-GeV}/c^2$* , Phys. Rev. Lett. **98** (2007) 012001, [arXiv:hep-ex/0603052](#).
- [8] J. Gaiser, *Charmonium Spectroscopy From Radiative Decays of the J/ψ and ψ'* , PhD thesis, SLAC, 1982.
- [9] LHCb, R. Aaij *et al.*, *Determination of the quark coupling strength $|V_{ub}|$ using baryonic decays*, [arXiv:1504.0156](#).
- [10] LHCb, R. Aaij *et al.*, *Study of the kinematic dependences of Λ_b^0 production in pp collisions and a measurement of the $\Lambda_b^0 \rightarrow \Lambda_c^+ \pi^-$ branching fraction*, JHEP **08** (2014) 143, [arXiv:1405.6842](#).

Erklärung:

Ich versichere, dass ich diese Arbeit selbstständig verfasst habe und keine anderen als die angegebenen Quellen und Hilfsmittel benutzt habe.

Heidelberg, den (Datum)